

THESIS

COMPOSITION OF FINE PARTICLES IN CARLSBAD CAVERNS NATIONAL PARK AND  
IMPLICATIONS FOR SOURCES AND VISIBILITY IMPACTS

Submitted by

Lillian E. Naimie

Department of Atmospheric Science

In partial fulfillment of the requirements

For the Degree of Master of Science

Colorado State University

Fort Collins, Colorado

Spring 2022

Master's Committee:

Advisor: Jeffrey L. Collett

Katherine B. Benedict

Emily V. Fischer

Shantanu Jathar

Copyright by Lillian E. Naimie 2022

All Rights Reserved

## ABSTRACT

### COMPOSITION OF FINE PARTICLES IN CARLSBAD CAVERNS NATIONAL PARK AND IMPLICATIONS FOR SOURCES AND VISIBILITY IMPACTS

The Carlsbad Caverns Air Quality Study (CarCavAQS) was designed to examine the influence of regional sources, including urban emissions, increased oil and gas development, wildfires and other biogenic sources, and soil dust on the park, including impacts on fine particle haze, ozone, and nitrogen deposition. Field measurements of aerosols, trace gases, and deposition were conducted from 25 July through 5 September 2019. Here the focus is on observations of the composition and concentration of fine particles and key trace gas precursors to understand important contributing species, their sources, and associated impacts on haze. Measurements focused on fine particulate matter (PM<sub>2.5</sub>) including mass, major ions, water soluble organic carbon (WSOC), and black carbon (BC) from various high time-resolution instruments as well as an Interagency Monitoring of Protected Visual Environments (IMPROVE) sampler. Supplemental measurements included denuder-filter pack sampling for inorganic gases (HNO<sub>3</sub> and NH<sub>3</sub>) and a Picarro cavity ring down spectrometer for methane (CH<sub>4</sub>). High-time resolution (6-minute) PM<sub>2.5</sub> mass ranged up to 31.8 µg m<sup>-3</sup>, with an average of 7.67 µg m<sup>-3</sup>. The main inorganic ion contributions were sulfate (avg 1.3 µg m<sup>-3</sup>), ammonium (avg 0.30 µg m<sup>-3</sup>), calcium (Ca<sup>2+</sup>) (avg 0.22 µg m<sup>-3</sup>), nitrate (avg 0.16 µg m<sup>-3</sup>), and sodium (avg 0.057 µg m<sup>-3</sup>). The WSOC average concentration was 1.2 µg C m<sup>-3</sup>. Inorganic ion concentrations had significant, sharp spikes in Ca<sup>2+</sup>, consistent with local dust generation and transport. Ion balance analysis suggests one period of acidic aerosol, the importance of ammonium and calcium in neutralizing sulfate, and significant reactions of nitric acid with sea salt and soil dust. The sums of PILS ion and WSOC concentrations, the latter multiplied by a factor of 1.8 to account for elements other than carbon, were not enough to reach mass closure with the TEOM PM<sub>2.5</sub> mass concentrations, suggesting that insoluble species are also an important

component of the aerosol at CAVE. IMPROVE sampler data, including insoluble species had good agreement between total  $\text{PM}_{2.5}$  mass and speciated  $\text{PM}_{2.5}$  aerosol mass. Sulfate is the major contributor to modeled light extinction in the 24-hour IMPROVE data set. Higher time resolution data had periods of significant light extinction from black carbon as well as sulfate, with a maximum 1-hour extinction value of  $90 \text{ Mm}^{-1}$ . Analysis of transport patterns indicated clear enrichment of sulfate, BC, and  $\text{CH}_4$  during periods when transport came from the southeast, the direction of greatest abundance of oil and natural gas development. Air masses transported from the northeast, a region of high agricultural activity, were enriched in ammonia.

## ACKNOWLEDGEMENTS

First I would like to thank my advisor, Jeff Collett, for the support and guidance throughout this process. I would like to thank Kathine B. Benedict, Emily V. Fischer and Shantanu Jathar for their willingness to serve on my committee. Thank you also to members of the Collett group, present and past. A special thank you to Katherine B. Benedict (now at Los Alamos National Laboratory) for her willingness to talk through concepts, provide feedback, and continued support. I would like to thank the officials at Carlsbad Caverns National Park for providing study access and logistical support, and my collaborators on this project: Amy P. Sullivan, Katherine B. Benedict, Anthony J. Prenni, Barkley Sive, Bret A. Schichtel, Emily V. Fischer, Ilana Pollack, and Jeffrey L. Collett. Thanks to Amy P. Sullivan and Katherine B. Benedict for their leadership of TEOM, URG, PILS-IC, PILS-WSOC, Picarro, and Aethalometer measurements. Thanks to Emily V. Fischer and Ilana Pollack for leadership of NO<sub>x</sub> measurements. Finally, thanks to Jeffrey Collett for his leadership as P.I. of this project. I would also like to thank the National Park Service for funding this project under Agreement Number P20AC00679 with Colorado State University. Finally I would like to thank my partner, Chloe Boehm, and dog, Astrid, for their support throughout this project and for convincing me to leave the lab and get outside everyday.

## TABLE OF CONTENTS

ABSTRACT . . . . .	ii
ACKNOWLEDGEMENTS . . . . .	iv
LIST OF TABLES . . . . .	vi
LIST OF FIGURES . . . . .	vii
Chapter 1 Introduction . . . . .	1
1.1 Oil and Natural Gas Production impacts on Air Quality . . . . .	1
1.2 Aerosol Formation . . . . .	5
1.3 Haze and Visibility in Protected Areas . . . . .	10
1.4 Carlsbad Caverns National Park . . . . .	14
Chapter 2 Methods . . . . .	16
2.1 Site Selection . . . . .	16
2.2 Measurements . . . . .	16
2.3 PILS IC/WSOC . . . . .	19
2.4 URG annular denuder and filter pack samplers . . . . .	20
2.5 IMPROVE . . . . .	22
2.6 Aethalometer . . . . .	22
2.7 Picarro . . . . .	23
2.8 TEOM . . . . .	24
2.9 NO <sub>xy</sub> Measurements . . . . .	24
2.10 IMPROVE Haze Algorithm . . . . .	24
2.11 HYSPLIT Residence Time Analysis . . . . .	25
Chapter 3 Results and Discussion . . . . .	27
3.1 Aerosol Composition . . . . .	27
3.2 Mass Closure and Visibility Impacts . . . . .	39
3.3 HYSPLIT Residence Time Analysis . . . . .	49
Chapter 4 Summary and Future Research Directions . . . . .	51
4.1 Summary . . . . .	51
4.2 Future Research Directions . . . . .	52
Appendix A USDA Census of Agriculture . . . . .	54
Appendix B Instrument Comparisons . . . . .	55
References . . . . .	57

## LIST OF TABLES

2.1	Table of Measurements . . . . .	18
3.1	Table of IMPROVE Soil Contributions . . . . .	46

## LIST OF FIGURES

1.1	U.S. dry natural gas production from 2000 to 2050. Taken from the U.S. Energy Information Administration. . . . .	2
1.2	Active oil and natural gas wells near Carlsbad Caverns National Park (CAVE) [HIFLD, 2019]. The color bar gives the number of active O/G wells in the given grid cell. The grid cell resolution is 0.1 degree by 0.1 degree and all cells with 500 or more active wells are shown with the same color. National Park boundaries are shown in green. Larger cities in the surrounding area are marked with black dots and labeled. The monitoring site in CAVE is shown as a yellow star. Coal-fired power plants are marked with a yellow plus sign [U.S. EIA, 2022a]. . . . .	15
2.1	Instrument inlets are shown above the CAVE Biology Office. Instruments sample from approximately 6 meters above ground level. . . . .	17
2.2	(a.) The experimental set-up for URG annular denuder/filter pack sampling is shown. Locations of the URG pump box, dry gas meter, and case which the sampling train is kept in are labeled. (b.) A sample train diagram, modified from the diagram in [Yu et al., 2005] is shown. . . . .	21
3.1	Timeseries of major PM <sub>2.5</sub> species and methane measured at the monitoring site. (a.) BC measured by the Aethalometer at 880 nm, WSOC measured by the PILS-TOC, and PM <sub>2.5</sub> measured by the TEOM. Note that there is a gap in the PILS-IC and PILS-TOC data at the beginning of the study period associated with a power outage . The BC and WSOC are plotted at a time-resolution of 2-minutes. TEOM total PM <sub>2.5</sub> is plotted at an hourly resolution. (b.) The five PILS-IC species with the largest contributions to total PM <sub>2.5</sub> are plotted at 30-minute time-resolution. (c.) CH <sub>4</sub> measured by the Picarro at 15-second time-resolution. . . . .	28
3.2	URG annular denuder/filter pack sampling shows the particle/gas phase partitioning of (a.) NH <sub>3</sub> and NH <sub>4</sub> <sup>+</sup> , (b.) HNO <sub>3</sub> and NO <sub>3</sub> <sup>-</sup> , and (c.) SO <sub>2</sub> and SO <sub>4</sub> <sup>2-</sup> . Particle species are shown in orange, and gas species are shown in blue. There is one day of missing data, 2019-08-04, due to a denuder extraction error. . . . .	30
3.3	PILS-IC species ammonium, sulfate, nitrate, and sodium are shown as nano equivalents per meter squared (nequiv. m <sup>-3</sup> ). (a.) Sulfate is shown in red and ammonium in green, (b.) shows nitrate in blue and sodium in purple, and (c.) shows calcium in orange and the sum of sulfate and nitrate in grey. . . . .	31
3.4	Fine particle sulfate is plotted against ammonium, both given in nequiv. m <sup>-3</sup> . The dotted grey line shows a slope of one. A simple linear regression was fitted to the purple data points and yielded a slope of 1.41 and R <sup>2</sup> of 0.66. The best fit line was forced through the origin and is shown in black. . . . .	32
3.5	Fine particle SO <sub>4</sub> <sup>2-</sup> and nitrate are both plotted against ammonium in nequiv. m <sup>-3</sup> . Each has an ordinary least squares linear regression plotted in black. The corresponding slope and R <sup>2</sup> values are next to the fits. . . . .	33

3.6	Fine particle nitrate is plotted against sodium, both given in nequiv. $\text{m}^{-3}$ . The dotted grey line shows a slope of one. A simple linear regression was fitted to the purple data points and yielded a slope of 1.37 and $R^2$ of 0.63. The best fit line was forced through the origin and is shown in black. . . . .	36
3.7	Fine particle chloride is plotted against sodium, both given in nequiv. $\text{m}^{-3}$ . The dotted grey line shows the expected ratio of chloride to sodium from sea water (1.164). A simple linear regression was fitted to the concentration data points and yielded a slope of 0.22 and $R^2$ of 0.55. The best fit line was forced through the origin and is shown in black. . . . .	37
3.8	The ratio of anion and cation species measured by the PILS-IC is plotted in equiv. $\text{m}^{-3}$ . The dotted grey line shows a ratio of unity. The blue points include ammonium and sodium for the cations, and the orange points add calcium to the cation species. The radius of the cation point size changes proportionally with calcium concentration.	38
3.9	48-hour HYSPLIT Back Trajectories are shown for three different transport patterns during the study. The dates were selected based on aerosol composition. 12 daytime (08:00-20:00) back trajectories of 48-hour duration are plotted for each date. . . . .	39
3.10	Speciated $\text{PM}_{2.5}$ measurements are shown as a sum, with the total $\text{PM}_{2.5}$ measured by the TEOM shown as a grey line. The sum of all species measured by the PILS-IC is shown in blue. Organic matter is shown in orange, estimated at 1.8 times the WSOC. Black carbon is shown in green from the Aethalometer at 880 nm. . . . .	40
3.11	IMPROVE $\text{PM}_{2.5}$ is plotted against TEOM $\text{PM}_{2.5}$ in $\mu\text{g m}^{-3}$ . The TEOM data set was resampled to a 24-hour mean and plotted for only the points with an IMPROVE. A least-squares linear regression shown in black was fitted to the data and forced through zero measurement. The grey dotted line is the 1:1 line, or $y=x$ . . . . .	41
3.12	IMPROVE mass closure is plotted in the upper panel, as the sum of OM, fine soil, ammonium sulfate, ammonium nitrate, and elemental carbon. The total $\text{PM}_{2.5}$ by mass is also shown by the black dots. (b.) The contribution to light extinction from each species plotted in (a.) as calculated using the second IMPROVE algorithm for light extinction. Site specific Rayleigh Scattering ( $10 \text{ Mm}^{-1}$ ) is included in addition to fine particle species. $\text{NO}_2$ (g) light extinction is calculated using the second IMPROVE algorithm and a resampled daily mean of the measured $\text{NO}_2$ . . . . .	42
3.13	Major $\text{PM}_{2.5}$ species are plotted from the IMPROVE and PILS-IC data sets. PILS-IC species were resampled to a daily mean and plotted for the days with an IMPROVE measurement. A least-squares linear regression was fitted to each set of points and forced through zero measurement. (a.) $\text{SO}_4^{2-}$ is compared between the data sets. IMPROVE $\text{SO}_4^{2-}$ was calculated directly from the given $(\text{NH}_4)\text{SO}_4$ . (b.) $\text{NO}_3^-$ is compared between the data sets. IMPROVE $\text{NO}_3^-$ was calculated directly from the given $\text{NH}_4\text{NO}_3$ . (c.) Sodium is compared between the data sets. (d.) Calcium is compared between the data sets. . . . .	45
3.14	IMPROVE OC is plotted against the PILS-WSOC measurement. WSOC was resampled to a daily average and plotted for only the days with IMPROVE measurements taken. A linear regression was fitted to the data and is shown in black. The slope of the least-squares linear regression is 1.09 and it has an $R^2$ of 0.64. The grey dashed line has a slope of 1. . . . .	47

3.15	PM <sub>2.5</sub> reconstructed light extinction is shown above. The second IMPROVE equation was applied to our higher time resolution composition data (PILS-IC, PILS-WSOC, Aethalometer BC and NO <sub>2</sub> ). These values include the Rayleigh background contribution (10 Mm <sup>-1</sup> ). The fractional light extinction contributions, excluding the site specific Rayleigh scattering, of the different species are shown for three data points (shown as blue triangles). Extinction peaks highlighting maximum contributions are represented by points a and c (30 July 2019 09:00 MST and 28 August 2019 12:00 MST). Point b represents a low light extinction period on 18 August 2019 12:00 MST.	48
3.16	Incremental probability distributions are plotted for 7 species measured directly during the field campaign: sulfate, ammonium, water-soluble organic carbon, calcium, nitrate, black carbon, and methane and 1 calculate value: light extinction (b <sub>ext</sub> ). The IPs are based on 24-hour back trajectories and are distance normalized. This is done by multiplying each grid cell value by the distance from the origin site, shown as a black dot. The grid cell resolution is 0.25 degrees square.	50
A.1	Total Agricultural Production is shown from the USDA Census of Agriculture in 2017. Each green dot corresponds to 10 million USD in agricultural production. Data can be found at: <a href="http://www.nass.usda.gov">www.nass.usda.gov</a>	54
B.1	Corresponding URG and PILS species are plotted at 24-hour time resolution. The PILS-IC data set was resampled to a daily mean. The dotted grey line has a slope of one and an intercept of zero.	55
B.2	Corresponding IMPROVE and PILS species are plotted at 24-hour time resolution. The dotted grey line has a slope of one and an intercept of zero.	56

# Chapter 1

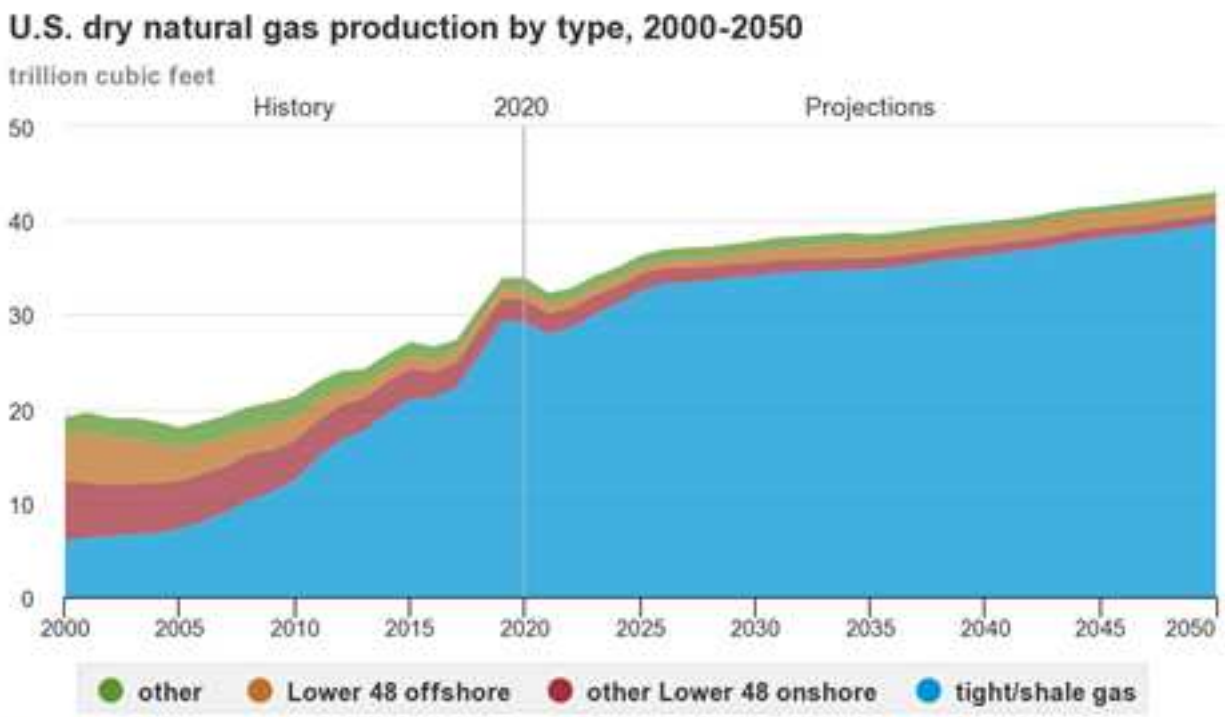
## Introduction

### 1.1 Oil and Natural Gas Production impacts on Air Quality

Air quality concerns are well established in relation to oil and natural gas (O/G) development. Most studies focus on gas phase pollutants, and the formation of ground level ozone. This work will focus on fine particulate matter, in a region close to heavy O/G development. To contextualize the air quality concerns about O/G development, it is important to understand the recent increases in O/G production, changes in extraction processes, related pollutants, and breadth of previous research.

O/G production increases in the United States are being driven by the extraction of previously inaccessible resources [U.S. EIA, 2021a]. This is largely due to the development of unconventional oil and natural gas extraction techniques, including horizontal drilling and hydraulic fracturing. Unconventional O/G extraction processes have led to a large increase in production from shale and tight oil and gas resources since 2000 [Brown et al., 2015]. Conventional vertical drilling can only cover a small surface area and targets O/G regions where the extracted products flow freely from the rock. Horizontal drilling allows one well pad to extract O/G from a much wider area where O/G is tightly bound in the underlying rock formation [U.S. EPA, 1999]. These tightly bound formations, shale, tight sands, and coal beds, require the rock to be broken apart by hydraulic fracturing to collect the O/G products [Olague, 2017]. After initiation of subsurface cracks in regions of hydrocarbon deposits, hydraulic fracturing (fracking) injects a pressurized combination of materials (water, proppant, and chemical additives) into the bed rock to enlarge and propagate those fissures to better release O/G from its tightly bound state. The fluids then flow back out of the fractures, leaving behind the proppant: sand suspended in the fluid to keep fractures open [Burden et al., 2015]. Shale gas resources can be found in almost 30 states across the U.S. [U.S. EIA, 2021a].

Tight oil production is driving the U.S. oil production growth. The two main source regions are the Bakken play in the Northern Great Plains and the Wolfcamp play in the Permian Basin, located in west Texas and south-east New Mexico [U.S. EIA, 2021a]. In 2010, U.S. crude oil production was 5.5 million barrels per day and grew to 12.2 million barrels per day in 2019 [U.S. EIA, 2021b]. Natural gas production in the U.S. has also climbed steeply, going from 19.1 trillion cubic feet in 2000 to 33.7 trillion cubic feet in 2019. The growth in natural gas production across the U.S. since 2000 is clear. Figure 1.1 shows that U.S. natural gas production is predicted to continue increasing until 2050 and the majority of that production will come from shale and tight gas resources [U.S. EIA, 2021a]. The U.S. Energy Information Administration, Annual Energy Outlook from 2021 also predicts that crude oil production in the U.S. will continue to rise through 2050.



Source: U.S. Energy Information Administration, *Annual Energy Outlook 2021 Reference case*, February 2021  
 Note: Other includes Alaska and coalbed methane

**Figure 1.1:** U.S. dry natural gas production from 2000 to 2050. Taken from the U.S. Energy Information Administration.

There are air quality concerns associated with unconventional oil and natural gas development specifically, and O/G more generally. Hydraulic fracturing and development of shale gas well pads can contaminate water resources near drill sites [Vengosh et al., 2014; Vidic et al., 2013]. Previous research has also looked extensively at air quality degradation from O/G through emission of toxic species and other air pollutants that contribute to production of photochemical smog [Field et al., 2015]. There are six EPA-regulated air pollutants produced as a result of O/G activity: ozone, particulate matter (PM<sub>2.5</sub>), carbon monoxide (CO), nitrogen oxides (NO<sub>x</sub>), sulfur oxide (SO<sub>x</sub>), and lead. Measurements in and around O/G development show well documented increased emissions of methane (CH<sub>4</sub>), volatile organic compounds (VOCs), and hazardous air pollutants (HAPs) from O/G development [U.S. EPA, 1999]. Emissions of VOCs and NO<sub>x</sub> from O/G operations have received attention due, in part, to their impacts on production of ozone [Brown et al., 2015; Field et al., 2015; Hecobian et al., 2019; Olaguer, 2012; Prenni et al., 2016; Thompson et al., 2014].

Tropospheric ozone is produced by oxidation of non-methane VOCs (NMVOCs) in the presence of NO<sub>x</sub> [Pandis and Seinfeld, 2016]. Ozone production can be limited by NMVOCs or NO<sub>x</sub>; O/G activities are a source of both sets of precursors. Tropospheric ozone is a criteria pollutant under the U.S. EPA and controlled by NAAQS (national ambient air quality standards). Ozone causes adverse respiratory effects when inhaled and can limit plant growth [Pandis and Seinfeld, 2016]. Regular emissions from O/G extraction have significant impacts on ozone formation in communities near extraction regions [Olaguer, 2012]. Although the production of ozone is often considered a summertime phenomenon, due to its dependence on light and temperature, O/G developments in the Upper Green River basin of Wyoming [Carter and Seinfeld, 2012; Field et al., 2015; Rappenglück et al., 2014; Schnell et al., 2009] and in the Uintah Basin of Utah [Ahmadov et al., 2015; Edwards et al., 2014; Oltmans et al., 2014] have been shown to drive wintertime ozone formation.

Methane emissions have been studied extensively due to the strong efficiency of methane as a greenhouse gas [Subramanian et al., 2015; Zimmerle et al., 2020]. Several investigators have also examined VOC emissions, due to impacts on production of ozone [Field et al., 2015; Prenni

et al., 2016; Thompson et al., 2014]. Methane emissions in particular have been tied to regular activities in O/G fields and to pervasive leaks and equipment failures [Lyon et al., 2016]. VOC species such as formaldehyde (HCHO) have been measured at considerable concentrations at O/G sites. One recent study found HCHO at times exceeding 100 ppb at a pipeline compressor station in Lake Arlington, Fort Worth (BSEEC study) [Olague, 2012]. Highly reactive VOCs (HRVOCs): ethene, propene, 1,3-butadiene, and butenes have been studied in particular because of their large impact on production of photochemical smog when emitted [Brown et al., 2015; Field et al., 2015; Hecobian et al., 2019; Olague, 2012; Prenni et al., 2016; Thompson et al., 2014]. These species have been targeted by a state implementation plan in Texas, in an attempt to reduce the impact of O/G activities on ozone production [Texas Commission on Environmental Quality]. Colorado has also promulgated air quality regulations on O/G activities to help limit emission of ozone precursors. When released in close proximity to NO<sub>x</sub> emissions from diesel engines (on-road and stationary) and flaring [Khalek et al., 2015], these species in particular have the potential to significantly increase ozone formation.

Specific VOC species have also been studied due to the associated increased risks of adverse health effects. Benzene, toluene, ethylbenzene, m-xylene, o-xylene, and p-xylene (BTEX) species have been considered for their acute exposure effects: skin and sensory irritation, central nervous system depression, respiratory problems [Brown et al., 2015] and because they are known carcinogens. These species were measured in high concentrations near O/G sites across the U.S. [Brown et al., 2015; Hecobian et al., 2019; McKenzie et al., 2012]. Recent work has also indicated a connection between elevated BTEX and other VOC species from O/G and an increased risk of cancer development, especially in communities chronically exposed to O/G emissions [McKenzie et al., 2012].

The associated emissions from O/G can be short term and variable and as such require a high measurement frequency. The highest exposures associated with O/G during a recent study in Texas, occurred during the drilling, flaring, and finishing processes [Brown et al., 2015], while study

of O/G VOC emissions in the Piceance and Denver-Julesburg Basins in Colorado were typically greatest during well flowback [Hecobian et al., 2019].

Flaring is the process by which excess gas production is burned away and has been associated with significant emissions of  $\text{NO}_x$ , BC, and  $\text{CH}_4$  during incomplete combustion [Allen et al., 2016; Böttcher et al., 2021; Conrad and Johnson, 2019; Weyant et al., 2016]. Flaring is an example by which O/G activities can emit particulate matter directly, in the form of BC. Oil and natural gas production are also responsible for the emission of gaseous precursors which can later lead to particle formation. However, few studies have looked directly at the particulate matter impacts from O/G development and their implications for other air quality constraints.

## 1.2 Aerosol Formation

Oil and natural gas development can emit particulate matter (PM) directly, emit gaseous precursors to particle formation and otherwise contribute to elevated PM. Research has indicated a significant impact on  $\text{PM}_{2.5}$  (particulate matter with a diameter of 2.5 micrometers and smaller) concentrations in areas near O/G development [Evanoski-Cole et al., 2017; Fann et al., 2018], although most emission inventories focus on gas phase species and ozone formation as discussed above.  $\text{PM}_{2.5}$  is a criteria pollutant under U.S. EPA regulations and has well-established adverse health impacts. Direct emissions of  $\text{PM}_{2.5}$  associated with O/G development include BC released during combustion processes, and anthropogenic increases to suspended mineral dust. Mineral dust emissions can be increased by O/G activities including truck traffic and alteration of soil surfaces [Pandis and Seinfeld, 2016].

Black carbon is emitted during O/G development by flaring and diesel engine use. Diesel trucks and on-site diesel engines are heavily used in oil and natural gas development areas [Bond et al., 2006; Khalek et al., 2015; Shen et al., 2021; Yanowitz et al., 2000]. On and off-road diesel engines contribute 70 percent of BC emissions in North America [Bond et al., 2013]. BC emissions have been reduced in recent years through effective controls; a recent study in China, for example, found recent diesel engine regulation changes to be effective in reducing BC directly emitted from

diesel vehicles [Shen et al., 2021]. However, BC emissions remain high around O/G development and production. Much of this black carbon comes from flaring; burning off excess gases from O/G production [Allen et al., 2016; Böttcher et al., 2021; Conrad and Johnson, 2019; Weyant et al., 2016]. Satellite data from 1994 through 2008 indicated that 140-170 billion cubic meters of natural gas was flared into the Earth's atmosphere each year during that time period [Elvidge et al., 2009]. It is likely that the amount of flared natural gas in the U.S. has increased since 2008 due to the increase in O/G production, the number of active wells, and the development of new O/G reserves located far from traditional infrastructure to transport recovered natural gas.

BC is of particular interest as a direct emission of O/G activities because of its strong absorption of solar radiation, in addition to the adverse health impacts of all  $PM_{2.5}$ . In general, the radiative forcing of BC has been estimated as second only to  $CO_2$  when considering the potential positive forcing and climate warming associated with atmospheric constituents [Bond et al., 2013]. The direct radiative forcing associated with BC is tied to its mass absorption cross section (MAC). A generic MAC value is often assumed for BC when calculating potential radiative forcing. However, flare generated BC has been shown to often have larger MAC values than other literature values associated with BC [Conrad and Johnson, 2019]. This could indicate that the radiative forcing associated with BC from flares could be larger than previously thought.

Other organic aerosol (OA) species can also be emitted or formed by atmospheric processes/reactions resulting in formation of secondary organic aerosol (SOA) [Pandis and Seinfeld, 2016]. Primary (directly emitted) organic aerosol (POA) species are emitted in the particle phase but some components have a high enough volatility that they quickly evaporate after emission as the source plume dilutes. Volatile, intermediate volatility (IV), or semi-volatile (SV) organic compounds can be oxidized to form lower volatility species which condense into the particle phase. This process can repeat, and OA can continue to undergo reactions and processes (oxidation, functionalization, polymerization) which decrease volatility and drive the OA into the particle phase [Pandis and Seinfeld, 2016]. The main pathway of SOA formation is the oxidation of VOC, IVOC, and SVOC species [Liggio et al., 2016]. SOA often makes up a majority of OA, and in the northern hemi-

sphere can account for greater than half the total  $\text{PM}_{2.5}$  mass [Zhang et al., 2007]. Due to the high emissions of VOCs associated with O/G development and production, SOA formation has received some attention in relation to O/G activity [Bahreini et al., 2012; Liggiio et al., 2016; Xiong et al., 2020].

O/G development and production also impact local to regional-scale levels of  $\text{SO}_4^{2-}$ , nitrate, and ammonium particulate species. This is partially through the direct emissions of  $\text{SO}_x$  and  $\text{NO}_x$  species. Sulfur dioxide ( $\text{SO}_2$ ) can be oxidized to form  $\text{H}_2\text{SO}_4$  (sulfuric acid) through both gas and aqueous phase reactions [Pandis and Seinfeld, 2016]. Similarly, emitted  $\text{NO}_x$  can be oxidized, via daytime or nighttime chemistry to form  $\text{HNO}_3$  [Pandis and Seinfeld, 2016]. Sulfuric and nitric acid can both react with gaseous ammonia, the most abundant atmospheric base, and form ammoniated sulfate and ammonium nitrate salts, respectively. Ammonium sulfate and ammonium nitrate are both hygroscopic particle species, with important implications for water uptake, total PM, particle size, and light scattering. The formation of both is highly dependent on thermodynamic conditions, and availability of ammonia.

If ammonia is very limited, sulfuric acid will exist in the particle phase. As the gaseous ammonia concentration increases, a series of compounds can form. These compounds include  $\text{NH}_4\text{HSO}_4$  (ammonium bisulfate),  $(\text{NH}_4)_3\text{H}(\text{SO}_4)_2$  (letovicite), and  $(\text{NH}_4)_2\text{SO}_4$  (ammonium sulfate). The composition of these ammoniated sulfate species changes as the molar ratio of ammonia to sulfuric acid changes. The formation of ammonium bisulfate is dominant with a ratio from 0.5 to 1.25, letovicite begins to form at a ratio of one and is dominant between 1.25 and 1.5, and the aerosol consists of almost entirely ammonium sulfate at a ratio of 2 [Pandis and Seinfeld, 2016]. Ammonium sulfate is the thermodynamically preferred state. If there is not enough ammonia to neutralize the sulfate present, the aerosol will be correspondingly acidic. Additional increases of ammonia (past a ratio of 2) lead to excess gaseous ammonia. Only once all the sulfate has been bound with ammonium do we expect to see significant formation of ammonium nitrate [Pandis and Seinfeld, 2016].

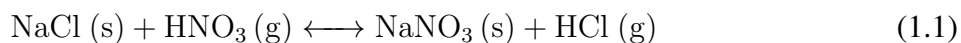
Ammonium nitrate is generally found in areas with high ammonia and nitric acid, but relatively low sulfate concentrations. It is formed through a gas phase reaction between ammonia and nitric acid, forming particle phase ammonium nitrate. However, ammonium nitrate can be solid or aqueous depending on the relationship between the ambient relative humidity (RH) and the salt's deliquescence RH (DRH) [Pandis and Seinfeld, 2016]. If the RH is less than the associated crystallization RH (CRH), ammonium nitrate will be a solid; when RH exceeds DRH, the ammonium nitrate will be in aqueous solution. Between the CRH and DRH values, ammonium nitrate may exist as a dry particle or a supersaturated solution, depending on the prior RH history. Low temperatures and high RH values both shift the ammonia-nitric acid system towards the aerosol phase, while hot, dry conditions shift the equilibrium toward the gas phase species.

Thermodynamic models can be used to further understand the SNA relationship and chemical composition under a set of given conditions. The aerosol inorganics model (AIM), created by Clegg, Wexler, and Brimblecombe [Clegg and Seinfeld, 2004; Wexler and Clegg, 2002; Wexler and Seinfeld, 1991], has been widely used for modeling inorganic aerosol ([www.aim.env.uea.ac.uk](http://www.aim.env.uea.ac.uk)). It calculates the gas, liquid, and solid partitioning in an aerosol system. It specifically considers the dominant inorganic particulate species: ammonium, sulfate, nitrate, sodium, and chloride. Another prevalent model for these calculations is ISORROPIA-II developed by Nenes, Pilinis, and Pandis [Fountoukis and Nenes, 2007; Nenes et al., 1998; 1999]. ISORROPIA-II is a thermodynamic equilibrium model looking at the  $K^+$  -  $Ca^{2+}$  -  $Mg^{2+}$  -  $NH_4^+$  -  $SO_4^{2-}$  -  $NO_3^-$  -  $Cl^-$  -  $H_2O$  aerosol system [Fountoukis and Nenes, 2007]. AIM makes fewer assumptions, whereas ISOPORRIA-II is less computationally costly. A recent study indicated that both models yield similar results across different input conditions [Hennigan et al., 2015].

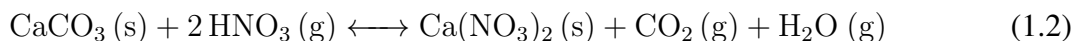
Some recent studies have indicated that the relationships and reactions described above can appear inconsistent with in situ observations. In the southeast U.S., for example, a 2016 study found that even with an excess of ammonia there was not full sulfate neutralization [Silvern et al., 2016]. The thermodynamic models described indicate that an equivalent-based ratio of ammonium to sulfate will be one, in the presence of enough ammonia. In the presence of excess ammonia,

measured ratios of these aerosol species have been lower than one [Attwood et al., 2014; Kim et al., 2015]. OA has been shown in the laboratory to slow the uptake of ammonia (g) by sulfate [Liggio et al., 2011]. This could potentially explain some observations in regions which have measured incomplete sulfate neutralization, even with excess gaseous ammonia [Kim et al., 2015; Silvern et al., 2016]. It is also possible that sulfate in such cases is in fact charge balanced, but fully or partially paired with cations other than ammonium. Sulfate could be present paired with soil dust cations, such as calcium in gypsum ( $\text{CaSO}_4$ ) erosion [Johnson, 1997].

Nitric acid (g) can also react with species other than ammonium to form nitrate aerosol. Sodium nitrate ( $\text{NaNO}_3$ ) aerosol will form when sea salt reacts with nitric acid as shown in Equation 1.1 [Pandis and Seinfeld, 2016]. This reaction is characterized by a chloride-deficient aerosol because hydrochloric acid has been displaced to the gas phase.



Equation 1.2 shows a different, soil dust reaction which can account for nitrate aerosol formation.



$\text{CaCO}_3$  and  $\text{HNO}_3$  are significantly reactive with each other at low RH values [Krueger et al., 2003]. Recent studies have found the calcium carbonate, nitric acid reaction to be important for nitrate aerosol formation [Fairlie et al., 2010; Jordan et al., 2003]. Calcium carbonate is the main constituent of limestone deposits and is found in dust particles due to erosion and soil composition. These two reactions can occur simultaneously to account for the formation of different composition nitrate aerosol. During the Big Bend Regional Aerosol and Visibility Observational (BRAVO), researchers found that nitrate was mostly associated with sea salt particle  $\text{Na}^+$ , but that the formation of calcium nitrate in reacted soil dust was also important on several days [Lee et al., 2004]. Calcium nitrate is a highly hygroscopic salt, so changes in state of nitrate and soil species need to be carefully considered when looking at haze [Krueger et al., 2003]. The formation of coarse

nitrate particles, often with a tail of the nitrate size distribution extending down to approximately 1  $\mu\text{m}$ , has also been reported for other locations across the U.S. [Lee et al., 2008]. This reaction is common where nitric acid is available in the gas phase, along with sea salt or soil dust particles, and ammonium nitrate is not thermodynamically favored due to insufficient ammonia and/or hot, dry conditions.

### 1.3 Haze and Visibility in Protected Areas

Class I protected areas have specific visibility requirements under the 1977 Clean Air Act. This act aims to protect National Parks and wilderness areas by preventing future visibility damage and decreasing current degradation. The Regional Haze Rule (RHR), enacted in 1999, calls for states and federal agencies to work on improving visibility impacts in the same protected areas [U.S. EPA, 1999]. The goal of the RHR is to reduce anthropogenic emissions to target improving the top 20 percent worst haze days and maintain the best 20 percent haze condition days across 156 national parks and wilderness areas [U.S. EPA, 1999]. The Interagency Monitoring or Protected Visual Environments (IMPROVE) network was started in 1985 to monitor visibility in these areas. Since 1985, the IMPROVE network has collected extensive long-term monitoring data in national parks and wilderness areas across the U.S.

Visibility degradation, or haze formation, results from the absorption and scattering of light by particle and gas phase species in the air. There are three types of haze structure: plume, uniform, and layered [Malm, 2016a]. Uniform haze forms when there is a sufficiently turbulent and therefore well mixed atmosphere. Plume and layered haze form when the atmosphere is stagnant, often happening during wintertime when the temperature and atmospheric turbulence are reduced. Haze is quantified by the loss of light along a given path and often quantified using a light extinction coefficient ( $b_{ext}$ ).  $B_{ext}$  represents the units of light lost per unit distance and is often given in inverse megameters ( $\text{Mm}^{-1}$ ). The light extinction coefficient is the sum of scattering and absorption light extinction coefficients. In the atmosphere, this can be further separated to the sum of scattering ( $b_{scat}$ ) and absorption ( $b_{abs}$ ) coefficients for both gases and particles, shown in Equation 1.3

[Malm, 2016b]. Scattering of gases and particles are shown as  $b_{sg}$  and  $b_{sp}$  respectively. Absorption of gases and particles are shown as  $b_{ag}$  and  $b_{ap}$  respectively.

$$b_{ext} = b_{scat} + b_{abs} = b_{sg} + b_{ag} + b_{sp} + b_{ap} \quad (1.3)$$

Although coarse mode particles (diameters larger than 2.5 micrometers) have large physical cross-sections and can comprise a substantial portion of total particulate matter mass, the scattering cross section is relatively larger for submicron particles due to their similarity in size to the wavelengths of visible light [Malm, 2016b]. These accumulation mode (0.1-1.0  $\mu\text{m}$ ) particles generally dominate total particle mass in polluted environments. Given their abundance and their large scattering cross sections, submicron particles typically account for the majority of visible light scattering. Gas phase species generally have much smaller contributions to visibility degradation, although  $\text{NO}_2(\text{g})$  absorbs blue light and can cause brown haze at sufficiently high concentrations. This effect is not common in most environments today.

The chemical composition of particulate matter further determines its effects on visibility. The major contributors to total  $\text{PM}_{2.5}$  mass are ammonium, sulfate, nitrate, organic matter, light absorbing carbon (black or elemental carbon), soil dust and sea salt. In considering visibility effects, soil and sea salt are approximated using the IMPROVE Algorithm. Soil is calculated based on Equation 1.4, and sea salt is calculated by Equation 1.5 [Malm et al., 2004].

$$\text{Fine Soil} = 2.2 * [\text{Al}] + 2.49 * [\text{Si}] + 1.94 * [\text{Ti}] + 1.63 * [\text{Ca}] + 2.42 * [\text{Fe}] \quad (1.4)$$

$$\text{Sea Salt} = 1.8 * [\text{Cl}^-] \quad (1.5)$$

Relative Humidity (RH) is also an important factor in determining visibility degradation because of the hygroscopic nature of sulfates, nitrates, and some organic species [Pandis and Seinfeld, 2016]. Water uptake at higher relative humidities increases particle size and associated light scattering.

The contributions of factors above led to the development of the IMPROVE algorithm to estimate light extinction based on RH, and species concentrations. The first algorithm assumes that gas absorption is negligible and includes only Rayleigh scattering for gas scattering. It further assumes that all sulfate is ammonium sulfate, and all nitrate is ammonium nitrate. Organic matter (OM) is calculated from measured organic carbon (OC) as shown in Equation 1.6.

$$[OM] = 1.4 * [OC] \quad (1.6)$$

The first IMPROVE algorithm uses a function of the RH value to determine a scale factor for water uptake growth of major hygroscopic species (ammonium sulfate and ammonium nitrate). Rayleigh scattering is assumed to be the same for all locations, at  $10 \text{ Mm}^{-1}$  [Pitchford et al., 2007]. This first IMPROVE algorithm tends to underestimate high values and overestimate low values when compared with nephelometer light extinction data [Pitchford et al., 2007].

Due to these errors in estimation, a second IMPROVE algorithm has been developed to better represent light extinction. Significant changes were made to improve the agreement: Rayleigh scattering was changed from one fixed value to a site-specific value, terms for sea salt and  $\text{NO}_2$  were added, the OM:OC scale factor was changed to 1.8 to better reflect current understanding of the importance of oxygenated organics, and some species were divided into two different size bins within the fine ( $\text{PM}_{2.5}$ ) mode to account for different light extinction properties based on size [Pitchford et al., 2007]. The new IMPROVE algorithm for light extinction is shown below. Hygroscopic species are multiplied by a growth factor, given as a function of relative humidity (RH). In Equation 1.7,  $f_S(\text{RH})$  and  $f_L(\text{RH})$  are prefactors calculated as a function of RH for the small bin, and large bins respectively. Sea salt has a corresponding prefactor calculated as a function of RH,  $f_{SS}(\text{RH})$ .

$$\begin{aligned}
b_{ext} = & 2.2 * f_S(RH) * [Small Ammonium Sulfate] \\
& + 4.8 * f_L(RH) * [Large Ammonium Sulfate] \\
& + 2.4 * f_S(RH) * [Small Ammonium Nitrate] \\
& + 5.1 * f_L(RH) * [Large Ammonium Nitrate] \\
& + 2.8 * [Small Organic Matter] \\
& + 6.1 * [Large Organic Matter] \\
& + 10 * [Elemental Carbon] \\
& + 1 * [Fine Soil] \\
& + 1.7 * f_{SS} * [Sea Salt] \\
& + Rayleigh Scattering (Site Specific) \\
& + 0.33 * [NO_2] \\
& + 0.6 * [Coarse Mass]
\end{aligned} \tag{1.7}$$

The large and small bins for ammonium sulfate, ammonium nitrate, and organic matter are estimated based on their mass concentration. If the mass concentration is greater than  $20 \mu\text{g m}^{-3}$ , all is estimated to be in the large mode. For masses less than  $20 \mu\text{g m}^{-3}$ , the large mode fraction is calculated as the total mass divided by  $20 \mu\text{g m}^{-3}$  [Pitchford et al., 2007]. The IMPROVE algorithm uses a site specific Rayleigh scattering value to calculate total light extinction above. The Rayleigh scattering value for CAVE is  $10 \text{ Mm}^{-1}$ . Coarse mass is the aerosol fraction between 2.5 and 10 microns. The contribution to light extinction from coarse mass aerosol is not considered for this work. Changing aerosol composition (reductions in sulfate and OM) in recent years has decreased agreement between light extinction values calculated using the second algorithm and measured nephelometer light extinction values [Prezzi et al., 2019], although the algorithm still provides a reasonable approximation under many conditions. Proximity to haze-causing sources (e.g., O/G flares) where a location can rapidly move from in-plume to out of plume is likely a cause of temporal variability in haze. Recent work shows rapid changes in aerosol composition

and concentration [Lee et al., 2008]. The 24-hour time resolution of the IMPROVE data set offers advantages to longer time scale analysis, however instruments which capture changes on the timescale of minutes to hours, which could be important for haze episodes.

## **1.4 Carlsbad Caverns National Park**

In this study, we examine impacts of O/G development and other sources on air quality in Carlsbad Caverns National Park (CAVE) in 2019. The park is located near extensive oil and natural gas development in the Permian Basin (Figure 1.2). The major formation in this region is the Wolfcamp shale play [Gaswirth et al., 2018]. This region is responsible for most of the shale gas production growth in the United States [U.S. EIA, 2021b]. Other potential sources (urban areas, major roadways, and coal-fired power plants) in the region are also shown in Figure 1.2. CAVE and the nearby town of Carlsbad frequently record high ozone values, often exceeding the 8-hr-average 70 ppbv National Ambient Air Quality Standard. A prior screening study of national parks in the southwestern U.S. [Benedict et al., 2020] revealed significant impacts of O/G emissions on VOC levels in CAVE, especially for light alkanes. The 2019 study in CAVE was motivated by these high ozone and VOC levels, along with concerns over sources of fine particle haze, and potential connection to a variety of regional sources including urban emissions, increased oil and gas development, wildfires, and erosion. Here we focus primarily on aerosol concentrations in the park, their contributions to regional haze, and their sources.

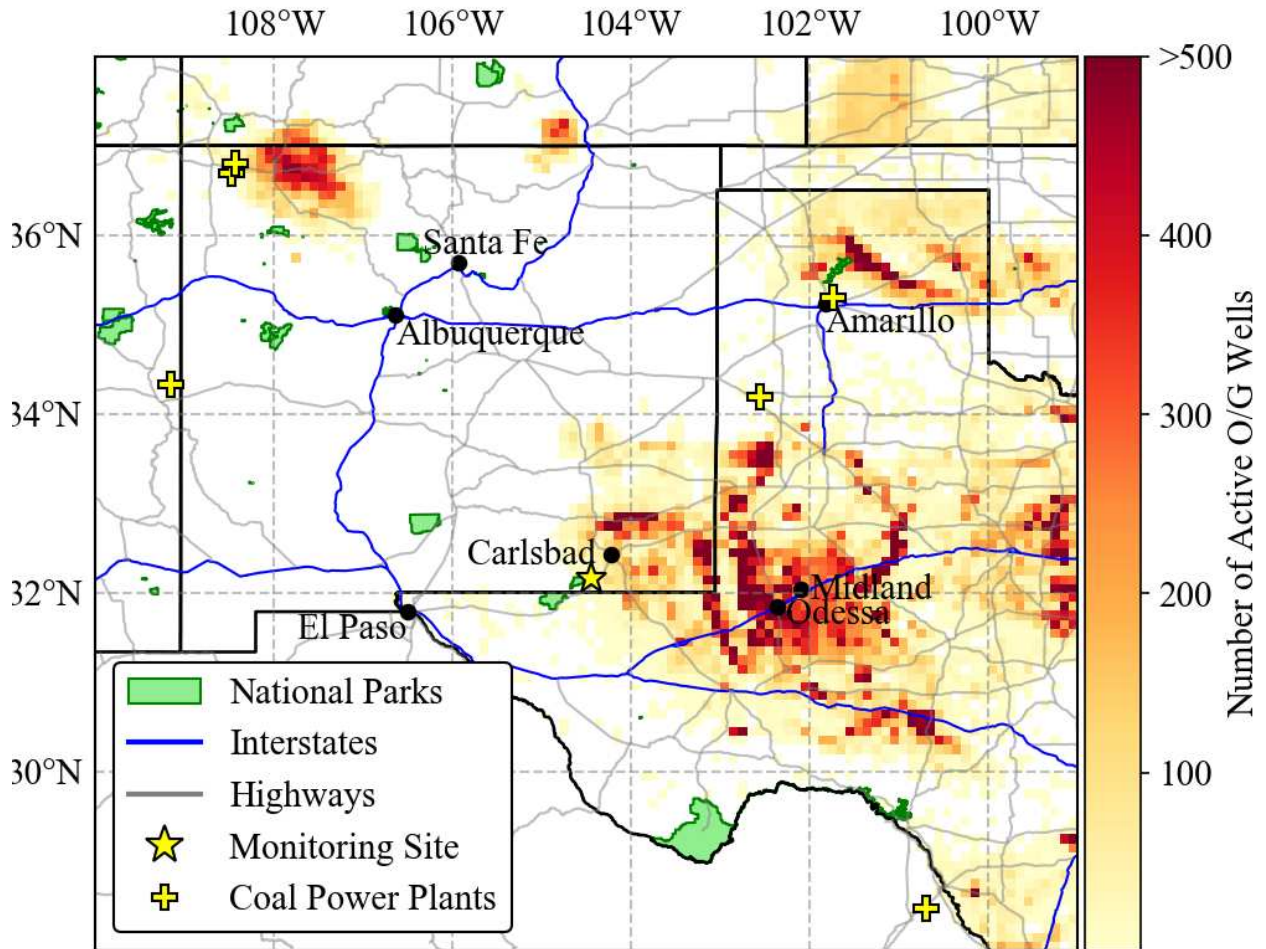


**Figure 1.2:** Active oil and natural gas wells near Carlsbad Caverns National Park (CAVE) [HIFLD, 2019]. The color bar gives the number of active O/G wells in the given grid cell. The grid cell resolution is 0.1 degree by 0.1 degree and all cells with 500 or more active wells are shown with the same color. National Park boundaries are shown in green. Larger cities in the surrounding area are marked with black dots and labeled. The monitoring site in CAVE is shown as a yellow star. Coal-fired power plants are marked with a yellow plus sign [U.S. EIA, 2022a].

# Chapter 2

## Methods

### 2.1 Site Selection

The Carlsbad Caverns Air Quality Study (CarCavAQS) was conducted at Carlsbad Caverns National Park (CAVE) in southeastern New Mexico from July 25 to September 5, 2019, to examine the influence of regional sources on fine particle haze, ozone, and nitrogen deposition in the park. Measurements were made outside of the CAVE Biology Office and building 58 (32.18° N, 104.44° W), located within the park, 0.5 km from the park visitor center. The altitude of the site location was approximately 1,355 meters. University Research Glassware (URG) denuder/filter pack cyclones were set at approximately 1 meter above ground level (agl), and all other instrument inlets sampled from approximately 6 meters agl. Instrument inlets are shown in Figure 2.1 below. The URG sampling set up is shown in Figure 2.2. Meteorological data were collected at the same site location, using the meteorological station 35-015-0010, operated by the National Park Service.

### 2.2 Measurements

Measurements of meteorological conditions, VOCs, ozone, PM<sub>2.5</sub>, other gas species, and nitrogen deposition were collected at different sampling integration periods. Here, our focus is primarily on characterization of aerosol mass and composition, along with concentrations of key trace gas species important either as aerosol precursors or as source indicators. The IMPROVE modules were installed as part of the IMPROVE network shortly before the intensive and continue to collect data; all other instruments collected data only for the duration of this intensive. The measurements used in this work and associated time resolutions are shown in Table 2.1.



**Figure 2.1:** Instrument inlets are shown above the CAVE Biology Office. Instruments sample from approximately 6 meters above ground level.

**Table 2.1:** Measurements made during the CarCavAQS study are listed with their respective time-resolutions and measured species. Only instruments used in this work are listed. Abbreviations used for the measured species: sodium ( $\text{Na}^+$ ), ammonium ( $\text{NH}_4^+$ ), calcium ( $\text{Ca}^{2+}$ ), potassium ( $\text{K}^+$ ), magnesium ( $\text{Mg}^{2+}$ ), chloride ( $\text{Cl}^-$ ), nitrite ( $\text{NO}_2^-$ ), nitrate ( $\text{NO}_3^-$ ), sulfate ( $\text{SO}_4^{2-}$ ), organic carbon (OC), black carbon (BC), elemental carbon (EC), ammonia ( $\text{NH}_3$ ), nitric acid ( $\text{HNO}_3$ ), sulfur dioxide ( $\text{SO}_2$ ), nitric oxide (NO), nitrogen dioxide ( $\text{NO}_2$ ), sum of reactive nitrogen oxides ( $\text{NO}_y$ ).

<i>Sampling Technique</i>	<i>Measured Species</i>	<i>Time Resolution</i>	<i>Limit of Detection</i>
<b><i>Aerosol</i></b>			
<i>URG filter pack</i>	PM <sub>2.5</sub> ions ( $\text{Na}^+$ , $\text{NH}_4^+$ , $\text{K}^+$ , $\text{Ca}^{2+}$ , $\text{Mg}^{2+}$ , $\text{Cl}^-$ , $\text{NO}_2^-$ , $\text{NO}_3^-$ , $\text{SO}_4^{2-}$ )	24-hour	0.01 $\mu\text{g m}^{-3}$
<i>Aethalometer</i>	PM <sub>2.5</sub> BC	2-minute	0.01 $\mu\text{g m}^{-3}$
<i>TEOM</i>	PM <sub>2.5</sub> mass	6-minute	0.1 $\mu\text{g m}^{-3}$
<i>PILS-IC</i>	PM <sub>2.5</sub> ions ( $\text{Cl}^-$ , $\text{NO}_3^-$ , $\text{SO}_4^{2-}$ , $\text{Na}^+$ , $\text{NH}_4^+$ , $\text{K}^+$ , $\text{Ca}^{2+}$ , $\text{Mg}^{2+}$ )	13-minute integrated sample every 30 minutes	0.08 $\mu\text{g m}^{-3}$ for $\text{Mg}^{2+}$ , 0.01 $\mu\text{g m}^{-3}$ for all other ions
<i>PILS-TOC</i>	PM <sub>2.5</sub> WSOC	2-minute	0.01 $\mu\text{g m}^{-3}$
<i>IMPROVE module A</i>	PM <sub>2.5</sub> mass and elemental composition	24-hour, every 3 <sup>rd</sup> day	0.3 $\mu\text{g m}^{-3}$ for PM <sub>2.5</sub> , 0.01-0.06 $\mu\text{g m}^{-3}$ for elemental analysis
<i>IMPROVE module B</i>	PM <sub>2.5</sub> ( $\text{Cl}^-$ , $\text{NO}_2^-$ , $\text{NO}_3^-$ , $\text{SO}_4^{2-}$ )	24-hour, every 3 <sup>rd</sup> day	0.001-0.01 $\mu\text{g m}^{-3}$
<i>IMPROVE module C</i>	PM <sub>2.5</sub> OC and EC	24-hour, every 3 <sup>rd</sup> day	0.1 $\mu\text{g m}^{-3}$ for OC and 0.02 $\mu\text{g m}^{-3}$ for EC
<b><i>Gases</i></b>			
<i>URG denuders</i>	Inorganic gases ( $\text{NH}_3$ , $\text{HNO}_3$ , $\text{SO}_2$ )	24-hour	0.01 $\mu\text{g m}^{-3}$
<i>Picarro Cavity Ringdown Spectrometer</i>	Methane	15-second	7 ppbv
<i>Eco Physics NO Analyzer</i>	NO, NO <sub>2</sub> , NO <sub>y</sub>	1-minute	20 pptv

## 2.3 PILS IC/WSOC

Particle-into-Liquid samplers (PILS) were used to measure the composition of water-soluble  $PM_{2.5}$  in near real-time. A PILS-Ion Chromatography (PILS-IC) system measured inorganic cations, anions, and low molecular weight organic acids [Sullivan et al., 2016] and a PILS-Total Organic Carbon (PILS-TOC) system measured water-soluble organic carbon (WSOC) [Sullivan et al., 2004, 2006]. The PILS mixes ambient particles with supersaturated water vapor to create droplets via heterogeneous nucleation and inertially capture  $PM_{2.5}$  [Orsini et al., 2003; Weber et al., 2001]. Each PILS sampled ambient air at 15 LPM using a 2.5  $\mu m$  size-cut inlet cyclone. Denuders coated with sodium carbonate and phosphorous acid were placed upstream of the PILS-IC to scrub out inorganic gases and an activated carbon parallel plate denuder [Eatough et al., 1993] was used to remove organic gases upstream of the PILS-TOC. For the PILS-TOC, to make a measurement of the background, a normally open actuated valve controlled by an external timer was periodically closed every 4 hours forcing the airflow through a Teflon filter before entering the PILS. The WSOC concentrations were calculated as the difference between the filtered and non-filtered measurements.

The PILS-IC system effluent was split to anion and cation Dionex ICS-1500 ICs. Both systems utilized an isocratic pump, self-regenerating suppressor, and conductivity detector. Both ICs completed an analysis every 30 minutes, with a sample loop fill time of 13 minutes. The cations were measured using a Dionex IonPac CS12A analytical (4  $\times$  250 mm) column with eluent of 18 mM methanesulfonic acid at a flowrate of 1.0 ml/min. A Dionex IonPac AS15 analytical (4  $\times$  250 mm) column using an eluent of 38 mM sodium hydroxide at a flowrate of 1.5 ml/min was used for the anion analysis. The ICs were calibrated using authentic standards before the study and a check standard was periodically injected during the study. The PILS-IC system measured  $Na^+$ ,  $NH_4^+$ ,  $K^+$ ,  $Ca^{2+}$ ,  $Cl^-$ ,  $NO_3^-$ , and  $SO_4^{2-}$  with a limit of detection of  $0.01 \mu g m^{-3}$  and magnesium with a LOD of  $0.08 \mu g m^{-3}$ .

In the PILS-TOC, to ensure insoluble particles were removed, the PILS liquid sample was pushed through a 0.2  $\mu m$  PTFE liquid filter using syringe pumps. The liquid was then sent to a

Sievers Model M9 Portable TOC Analyzer (Suez Water Technologies and Solutions, Treviso, PA). This instrument oxidizes organic carbon (OC) to CO<sub>2</sub> using ammonium persulfate and ultra-violet light. The carbon dioxide formation is measured using a conductivity sensor. The amount of OC measured is proportional to the conductivity increase. The instrument was used in on-line mode with a 2-minute integration time. The TOC Analyzer was calibrated in the factory and periodically verified by analysis of oxalic acid standards.

## **2.4 URG annular denuder and filter pack samplers**

University Research Glassware (URG) annular denuder and filter pack samplers were used to measure inorganic gas and particle species [Allegrini et al., 1987, 1994; Fitz, 2021]. The air flow passed through a Teflon coated PM<sub>2.5</sub> cyclone then through a sodium bicarbonate coated annular denuder to collect HNO<sub>3</sub> (g) and SO<sub>2</sub> (g), a phosphorous acid coated denuder to collect NH<sub>3</sub> (g), and a 37 mm nylon filter (MTL Nylasorb, 1.0 μm pore size) to capture PM<sub>2.5</sub> particles. Finally, an additional phosphorous acid coated denuder is located downstream of the filter to capture any NH<sub>3</sub> volatilized from ammonium nitrate initially captured on the filter. The filter effectively retains nitric acid from this reaction, due to the nylon filter's affinity for HNO<sub>3</sub> [Benedict et al., 2013; Lee et al., 2008; Yu et al., 2005, 2006]. The flow was controlled at 10 L min<sup>-1</sup> and the pressure drop across the sampling train was recorded. A dry gas meter downstream of the sample train measured the total flow integrated across the sampling period, which was then corrected for the pressure drop to obtain the ambient sample volume. URG samples were collected every 24 hours, from midnight to midnight. The sampling train is shown in Figure 2.2b.

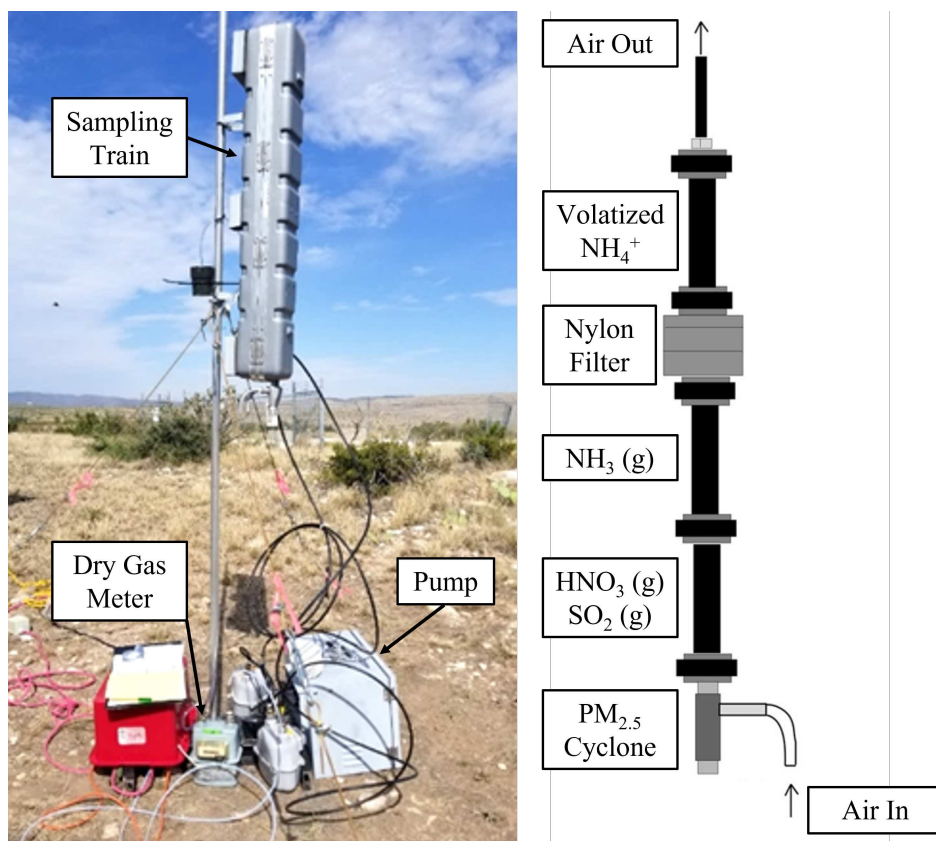


**Figure 2.2:** (a.) The experimental set-up for URG annular denuder/filter pack sampling is shown. Locations of the URG pump box, dry gas meter, and case which the sampling train is kept in are labeled. (b.) A sample train diagram, modified from the diagram in [Yu et al., 2005] is shown.

After sample collection, annular denuders and filters were extracted in 10 mL and 6 mL 18.2 MΩ deionized water, respectively. Samples were then analyzed for anion and cation species using ion chromatography. Both systems utilized a Dionex DX-500 ion chromatograph (IC), which includes an isocratic pump, self-regenerating anion or cation suppressor, and conductivity detector. The injection volume of both methods was 50 μL and analysis time was 17 minutes. The anion IC was used to quantify gas species (HNO<sub>3</sub>, SO<sub>2</sub>), and PM<sub>2.5</sub> species (Cl<sup>-</sup>, NO<sub>2</sub><sup>-</sup>, NO<sub>3</sub><sup>-</sup>, and SO<sub>4</sub><sup>2-</sup>). An IonPac AS14A (4×150 mm) analytical column was used with 1 mM sodium bicarbonate and 8 mM sodium bicarbonate eluent at a flow rate of 1 mL min<sup>-1</sup>. The cation IC was used to quantify gaseous ammonia (NH<sub>3</sub>), and PM<sub>2.5</sub> species: Na, NH<sub>4</sub><sup>+</sup>, K<sup>+</sup>, Mg<sup>2+</sup>, Ca<sup>2+</sup>. A Dionex IonPac CS12A (3×120 mm) analytical column was used with 20 mM methanesulfonic acid eluent at a flow

rate of  $0.5 \text{ mL min}^{-1}$ . Each component was quantified using an 8-standard calibration curve. A standard replicate and blank sample were analyzed after every 10 samples. Based on previous work the relative standard deviations (RSDs) of major aerosol ion concentration measurements ( $\text{NO}_3^-$ ,  $\text{SO}_4^{2-}$ , and  $\text{NH}_4^+$ ) are estimated to be between 3-5 percent and the RSDs for replicate denuder gas concentration measurements are estimated to be approximately 10 percent [Lee et al., 2004].

## 2.5 IMPROVE

The Interagency Monitoring of Protected Visual Environments (IMPROVE) network was developed to look at visibility impacts and emissions impacting Class I national parks and wilderness areas. IMPROVE monitoring sites consist of four modules (A, B, C, and D) to measure particulate matter. Modules A, B, and C measure  $\text{PM}_{2.5}$  and provide the data sets considered in this work. Module A collects  $\text{PM}_{2.5}$  on a Teflon filter, which is then analyzed gravimetrically for  $\text{PM}_{2.5}$  mass and by x-ray fluorescence (XRF) for elemental composition [Prenni et al., 2016]. The XRF analysis quantifies all elements including and between Na (atomic number 11) and Pb (atomic number 82). Module B collects  $\text{PM}_{2.5}$  on a nylon filter, analyzed by IC for  $\text{SO}_4^{2-}$ ,  $\text{NO}_3^-$ ,  $\text{NO}_2^-$ , and  $\text{Cl}^-$  concentrations. Module C collects  $\text{PM}_{2.5}$  on a quartz filter that is analyzed by thermal optical reflectance (TOR) for OC and EC concentrations [Malm et al., 2004; Chow et al., 2007]. The filters are incrementally heated to volatilize first OC and then EC, making use of defined temperature steps and controlling the chamber atmosphere; the carbon molecules are converted to  $\text{CO}_2$ , which is then analyzed by a non-dispersive infrared detector [Malm et al., 2004]. The detector response gives OC and EC concentrations and includes optical correction for OC charring prior to EC evolution. Module D collects  $\text{PM}_{10}$  on a Teflon filter and determines the total  $\text{PM}_{10}$  gravimetrically. Further documentation can be found on the IMPROVE website (<http://vista.cira.colostate.edu/Improve/>).

## 2.6 Aethalometer

A Magee-Scientific 7-channel Aethalometer (model AE31) measured  $\text{PM}_{2.5}$  light absorbing carbon at seven different wavelengths: 350, 470, 520, 590, 660, 880, and 950 nm [Hansen et al.,

1984]. Ambient air is drawn through a quartz fiber filter tape and particles are collected. The light attenuation at that location is then compared to an un-exposed tape, to calculate optical absorption of the collected particles. An increase in light attenuation from the sampled location corresponds to an increase in collected light absorbing carbon. The different wavelengths can be used individually or together for additional analysis [Duc et al., 2020]. Absorption at 880 nm was used to determine the BC concentration [Drinovec et al., 2015]. BC is characterized by its ideal absorption of visible light and is predominantly formed through incomplete combustion processes. Elemental carbon is also made of entirely carbon atoms. Both BC and EC are operationally defined and can have somewhat different chemical and physical properties. Petzold et al. [2013] proposes that BC or equivalent black carbon (EBC) be used for data collected using optical absorption methods. The aethalometer is one such method and will be reported in this work as BC concentration. The aethalometer was operated using the standard procedure provided elsewhere [Petzold et al., 2013].

## 2.7 Picarro

A Picarro gas concentration analyzer (G2508) was used to quantify gas concentration of methane ( $\text{CH}_4$ ), carbon dioxide ( $\text{CO}_2$ ), and ammonia ( $\text{NH}_3$ ) every 15 seconds. The instrument also measures water vapor, used to automatically correct data for changes in detection due to overlapping absorbance by water vapor. All species are detected using cavity ring-down spectroscopy (CRDS). This technique relies on the unique near-infrared absorption spectrum of these gas phase molecules. A single frequency laser diode enters a cavity with three mirrors arranged to create a continuous traveling light wave. The reflections between mirrors create an extended path length to limit the signal to noise ratio and improve detection from the instrument. After a threshold is reached by the photodetector, the laser is shut off. The rate at which the light decays in the cavity (ring-down) is accelerated by the presence of target gas species. That decay is compared to the ring-down time without additional absorption by the target gas, to calculate the gas phase concentration. Methane concentration was measured with  $<7$  ppb precision at 1-minute time resolution. The Picarro sampled from a  $\frac{1}{4}$ " heated Teflon line, to limit the loss of gaseous ammonia, and through a fiber filter

at its inlet, to remove particles. Before deployment the calibration was verified by injection of known concentrations diluted from certified cylinders. Zero measurements were made weekly by overflowing the inlet with ultra-high purity zero air for 30 min.

## 2.8 TEOM

A Tapered Element Oscillating Microbalance (TEOM, model 1405-DF) from Thermo Scientific was used to measure the  $PM_{2.5}$  mass concentration [Clements et al., 2013]. Only  $PM_{2.5}$  data from the TEOM was used due to the configuration of the inlet which was not designed to fully transmit larger particles. The TEOM 1405-DF uses diffusion rather than heated drying to better retain and capture semi-volatile species in the particles. The TEOM is a gravimetric instrument. It draws air through a filter, at a constant flow rate and periodically weighs the filter to calculate mass change and thus the mass concentration of the collected particles. The mass is detected as a frequency change in the oscillation of a tube holding the filter cartridge. As such, the mass is determined based on the inertia changes of the oscillating tube. One major advantage of this method is that changes in aerosol characteristics do not influence the accuracy of the mass measurement. The TEOM measurement resolution is  $0.1 \mu\text{g m}^{-3}$ . The TEOM was calibrated in the field with a standard calibration filter from the manufacturer.

## 2.9 $NO_{xy}$ Measurements

An Eco Physics NO (nitric oxide) analyzer coupled with inlets built by Dr. Ilana Pollack detected NO,  $NO_2$ , and  $NO_y$ , using NO- $O_3$  chemiluminescence.  $NO_2$  was converted to NO by 395 nm photolysis [Pollack, 2010] and  $NO_y$  was converted to NO by a molybdenum converter heated to 320 C. For more information, contact Dr. Ilana Pollack (ipollack@rams.colostate.edu).

## 2.10 IMPROVE Haze Algorithm

The chemical composition of particulate matter, which determines the particle refractive index and hygroscopicity, is a key factor influencing light extinction. Potentially major contributors to

total  $PM_{2.5}$  mass are ammonium sulfate, ammonium nitrate, organic matter, light absorbing carbon (black or elemental carbon), soil dust and sea salt. The second IMPROVE algorithm shown in Equation 1.7, calculates  $b_{ext}$  the light extinction, including particle light scattering and terms for Rayleigh scattering and  $NO_2$  (g) light extinction. Coarse mass light extinction is not considered in this work. Changing aerosol composition, specifically a reduction in sulfate and organic matter (OM), in recent years has decreased the agreement between the second algorithm and measured nephelometer light extinction values [Prenni et al., 2019], although it is still a reasonable approximation under many conditions.

## 2.11 HYSPLIT Residence Time Analysis

The National Oceanographic and Atmospheric Administration Air Resource Laboratory Hybrid Single-Particle Lagrangian Integrated Trajectory (HYSPLIT) model [Stein et al., 2015] was used to calculate back trajectories initiated from the CAVE monitoring site. Trajectories were generated for every hour of the study period, and each went back 24 or 48 hours. The HYSPLIT endpoint time step was 1 hour. This work looks at air parcel back trajectories to determine air mass origin location and source-receptor relationships. The HYSPLIT model is a hybrid between a Lagrangian approach and Eulerian approach and uses input meteorological model data to determine the path an air parcel took. NAM-12 meteorological data were used. This model has 12 km horizontal resolution, 26 atmospheric levels, and a 3-hour frequency. The HYSPLIT vertical motion parameter was set to take vertical velocity fields directly from the meteorological model, the model top was set at 10,000 m-agl (meters above ground level), and the parcel was initiated at 10 m-agl. Only the first ensemble trajectory was used.

The generated HYSPLIT trajectories and source-receptor relationships were investigated using Residence Time Analysis (RTA) [Gebhart et al., 2018, 2021]. The residence time is the amount of time that a parcel spends in a horizontal grid-cell. This can be calculated as a probability, called the everyday probability (EP). Grid cells were defined with a  $0.25^\circ$  resolution. In Equation 2.1,  $n_{ij}$  represents the total endpoints passing through grid cell  $i,j$ , and  $N$  represents the total endpoints

passing through all grid cells. Grid cells were defined with a 0.25° resolution.

$$EP = \frac{n_{ij}}{N} \quad (2.1)$$

High concentration residence times, or high probabilities (HP) are calculated using trajectories from the top 10 percent of concentration values measured at the receptor site. The top 10 percent of all concentration data points were verified to be greater than one standard deviation from the mean, to ensure they appropriately represented high values. The high probability (HP) residence time calculation is shown in Equation 2.2 where  $m_{ij}$  represents the total high endpoints passing through grid cell  $i,j$ , and  $M$  represents the total high endpoints passing through all grid cells.

$$HP = \frac{m_{ij}}{M} \quad (2.2)$$

These two residence times can be compared using the incremental probability (IP): the difference between HP and EP (Equation 2.3). The IP gives a comparison between HP and EP to determine if the probability of an endpoint being in a grid cell is more likely on a high probability period or throughout the data set.

$$IP = HP - EP \quad (2.3)$$

# Chapter 3

## Results and Discussion

### 3.1 Aerosol Composition

To examine impacts of O/G and other sources on air quality in CAVE, various measurements are combined to look at the frequency and types of elevated PM<sub>2.5</sub> events. Our analysis focuses on carbonaceous aerosol, inorganic ions, and total PM<sub>2.5</sub>. The timelines of PM<sub>2.5</sub> components measured at high-time resolution are shown in Figure 3.1, with hourly average total PM<sub>2.5</sub> mass. Episodic increases of many of the species are observed, but the duration and frequency of these events varies. Hourly averaged PM<sub>2.5</sub> ranged up to 27  $\mu\text{g m}^{-3}$  (maximum of 31.8  $\mu\text{g m}^{-3}$  at 6-minute resolution) and had an average value of 7.67  $\mu\text{g m}^{-3}$ . Figure 3.1 (a.) shows water-soluble organic carbon and black carbon, which had average concentrations of 1.2  $\mu\text{g C m}^{-3}$  and 0.48  $\mu\text{g m}^{-3}$ , respectively.

Several BC spikes exceeded 4  $\mu\text{g m}^{-3}$ . Although biomass burning can influence CAVE in summer, elevated BC measured in this campaign is likely not from biomass burning given low concentrations of levoglucosan, a good tracer for biomass burning [Sullivan et al., 2008], measured throughout the study. To investigate the other sources of the episodic BC increases, the NO/NO<sub>x</sub> ratio and methane mixing ratio were used. When the emitted NO<sub>x</sub> is almost entirely NO (a NO to NO<sub>x</sub> ratio close to 1) a locally generated combustion plume is suggested. None of the BC spikes correspond with NO/NO<sub>x</sub> ratios greater than 0.32 (daytime avg. 0.2), at 2-minute time resolution, indicating that the elevated BC values do not come from local sources. Methane mixing ratio is shown in Figure 3.1 (c.) and had an average value of 2.1 ppmv. The methane mixing ratio was greater than one standard deviation (0.16 ppmv) above the mean for all BC values above 4  $\mu\text{g m}^{-3}$ , implying that these high BC values could be associated with O/G flaring and diesel engine use. The largest BC value (2019-07-27 08:48:00 MST) corresponds to a gap in other PM<sub>2.5</sub> data. The NO/NO<sub>x</sub> ratio for this point was 0.1, and methane mixing ratio was 2.1 ppmv. The low NO/NO<sub>x</sub>

ratio implies that this largest BC value does not come from an idling truck or other source near the aethalometer sampling inlet.

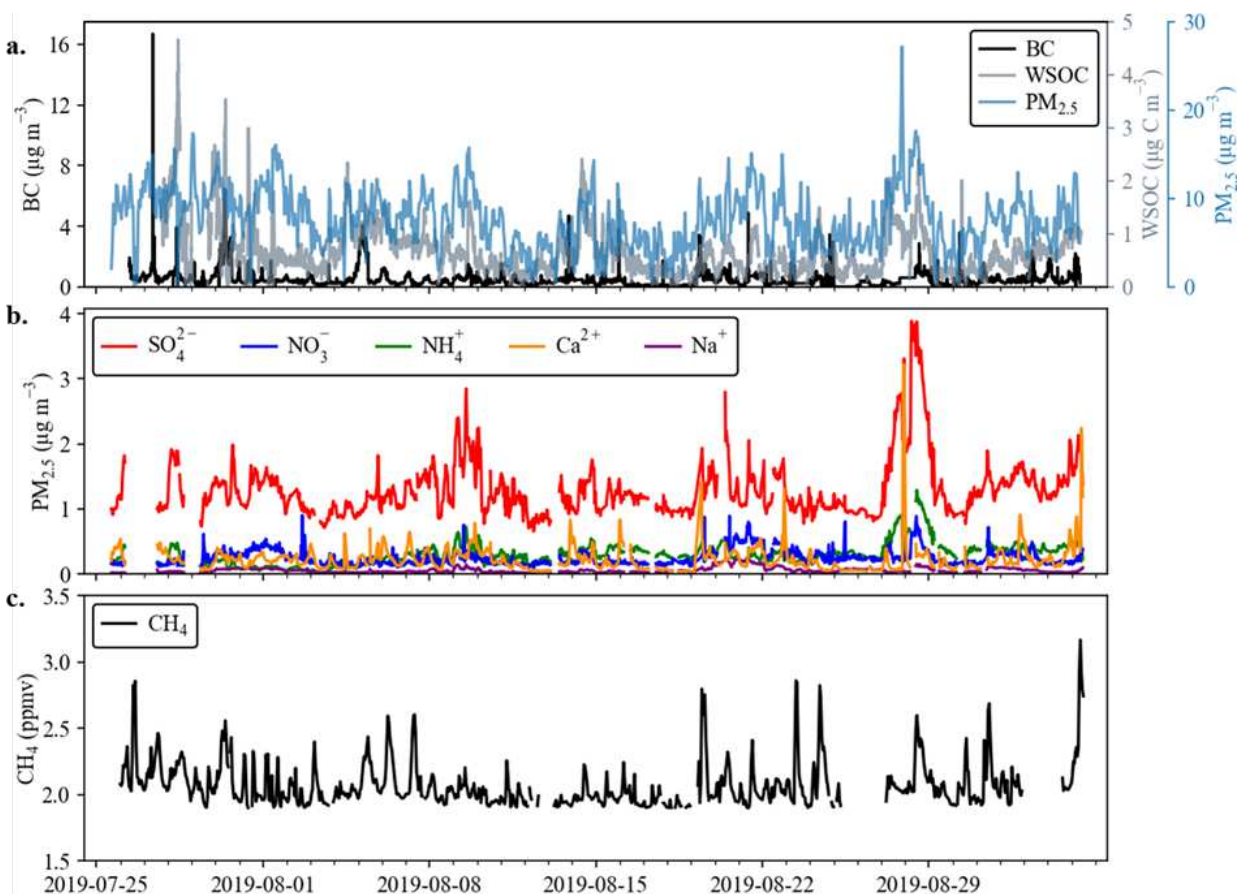


**Figure 3.1:** Timeseries of major PM<sub>2.5</sub> species and methane measured at the monitoring site. (a.) BC measured by the Aethalometer at 880 nm, WSOC measured by the PILS-TOC, and PM<sub>2.5</sub> measured by the TEOM. Note that there is a gap in the PILS-IC and PILS-TOC data at the beginning of the study period associated with a power outage. The BC and WSOC are plotted at a time-resolution of 2-minutes. TEOM total PM<sub>2.5</sub> is plotted at an hourly resolution. (b.) The five PILS-IC species with the largest contributions to total PM<sub>2.5</sub> are plotted at 30-minute time-resolution. (c.) CH<sub>4</sub> measured by the Picarro at 15-second time-resolution.

Figure 3.1 (b.) shows timelines of the highest concentration PM<sub>2.5</sub> species measured by the PILS-IC: SO<sub>4</sub><sup>2-</sup> (avg 1.3  $\mu\text{g m}^{-3}$ ), NH<sub>4</sub><sup>+</sup> (avg 0.30  $\mu\text{g m}^{-3}$ ), Ca<sup>2+</sup> (avg 0.22  $\mu\text{g m}^{-3}$ ), NO<sub>3</sub><sup>-</sup> (avg 0.16  $\mu\text{g m}^{-3}$ ), and Na<sup>+</sup> (avg 0.057  $\mu\text{g m}^{-3}$ ). The calcium timeline exhibits several short term, concentration spikes reaching as high as 3.2  $\mu\text{g m}^{-3}$ . This could be associated with soil dust from local erosion of limestone or gypsum deposits. There are significant gypsum (CaSO<sub>4</sub>) and dolomite

(CaCO<sub>3</sub>) deposits in the Permian Basin [Johnson, 1997], located near the Carlsbad Caverns monitoring site. Gypsum is a mineral made of calcium and sulfate and could explain at least some of the sulfate and episodically elevated calcium concentrations. A significant proportion of the sulfate in White Sands National Park, another National Park in the area, was contributed by gypsum and other salts in the area during a recent study [White et al., 2015]. The presence of CaSO<sub>4</sub> and/or CaCO<sub>3</sub>, is likely the main source of Ca<sup>2+</sup>, is challenging to directly confirm because sulfate has other anthropogenic sources and carbonate cannot be measured directly on the PILS-IC. The role of calcium in the aerosol chemistry will be investigated further below.

Ammonium, nitrate, and sulfate and their gas phase counterparts, ammonia, nitric acid, and sulfur dioxide, were also measured at a daily time resolution by the URG denuder/filter pack samplers, as shown in Figure 3.2. Study average concentrations are given for gas phase measurements: NH<sub>3</sub> (avg 0.93 μg m<sup>-3</sup>), HNO<sub>3</sub> (avg 0.89 μg m<sup>-3</sup>), and SO<sub>2</sub> (avg 0.64 μg m<sup>-3</sup>), and PM<sub>2.5</sub> measurements: NH<sub>4</sub><sup>+</sup> (avg 0.47 μg m<sup>-3</sup>), NO<sub>3</sub><sup>-</sup> (avg 0.27 μg m<sup>-3</sup>), and SO<sub>4</sub><sup>2-</sup> (avg 1.3 μg m<sup>-3</sup>). For ammonia/ammonium and, especially, nitric acid/nitrate, the system was dominated by the gas phase constituent throughout the study period. In the case of gaseous sulfur dioxide and PM<sub>2.5</sub> SO<sub>4</sub><sup>2-</sup>, most days saw greater abundance of the particle phase component. As discussed earlier, sulfate aerosol will tend to form ammonium sulfate if there is sufficient ammonia gas present. The presence of excess gaseous ammonia from the denuder collection would indicate that ammoniated sulfate salts are likely to be present as ammonium sulfate, rather than more acidic ammonium bisulfate or letovicite. The presence of significant gas phase HNO<sub>3</sub> and NH<sub>3</sub> illustrates the potential for additional formation of particle nitrate, either ammonium nitrate formation under cooler more humid conditions, perhaps at other times of year, or additional coarse particle nitrate resulting from further nitric acid reactive uptake on sea salt or soil dust particles.

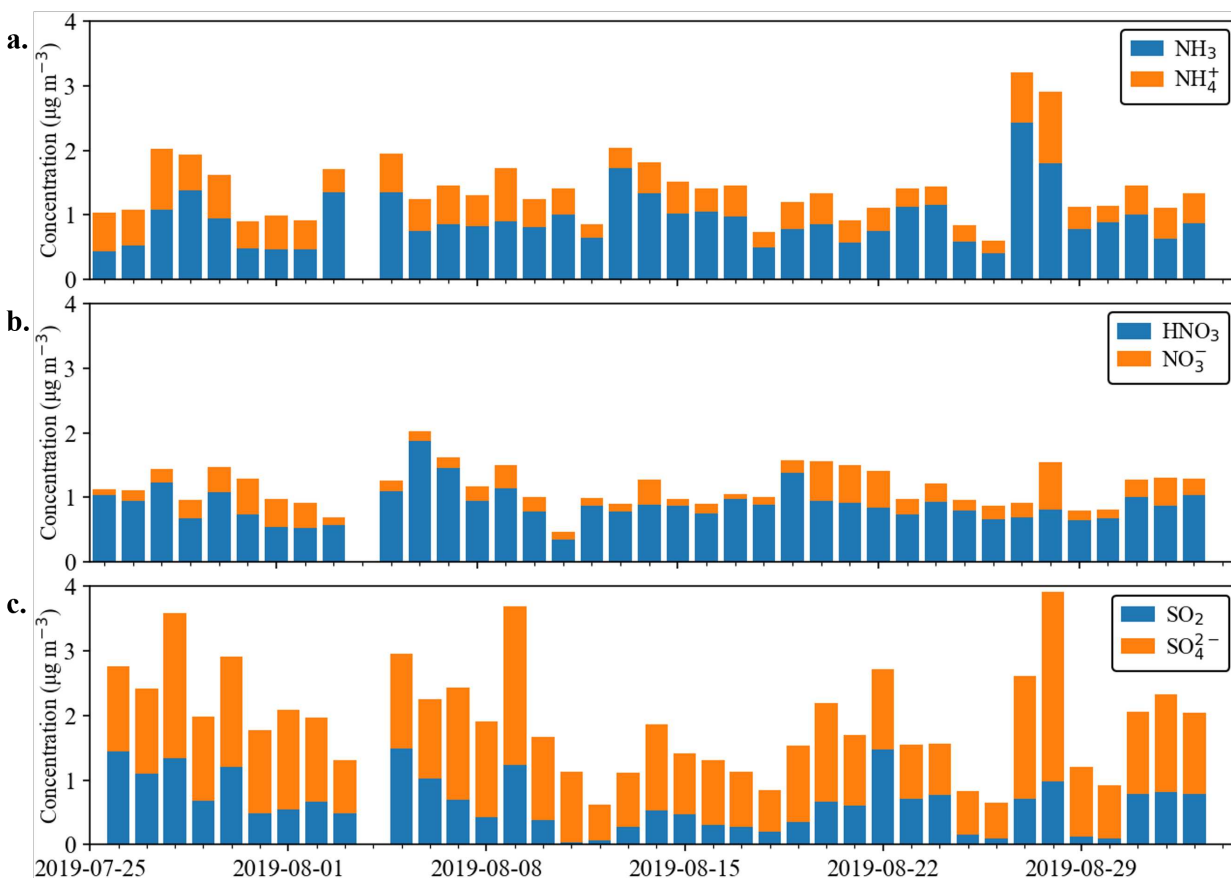


**Figure 3.2:** URG annular denuder/filter pack sampling shows the particle/gas phase partitioning of (a.)  $\text{NH}_3$  and  $\text{NH}_4^+$ , (b.)  $\text{HNO}_3$  and  $\text{NO}_3^-$ , and (c.)  $\text{SO}_2$  and  $\text{SO}_4^{2-}$ . Particle species are shown in orange, and gas species are shown in blue. There is one day of missing data, 2019-08-04, due to a denuder extraction error.

Four of the major PILS-IC species are re-plotted in Figure 3.3, in concentration units of nano equivalents per meter cubed, to better assess issues related to ion charge balance. Figure 3.3 (a.) indicates that  $\text{PM}_{2.5}$  sulfate is only partially neutralized by ammonium, with an average ammonium to sulfate charge equivalent ratio of 0.6. 24-hour gaseous ammonia measured using the URG annular denuders averaged  $0.93 \mu\text{g m}^{-3}$  (Figure 3.2). One would typically expect acidic sulfate aerosol (e.g., sulfuric acid or ammonium bisulfate) to take up gaseous ammonia if available. The coexistence of gaseous ammonia with sulfate not fully neutralized by ammonium may indicate the presence of a different sulfate particle species. Figure 3.3 (b.) indicates that much of the  $\text{NO}_3^-$  may be present as  $\text{NaNO}_3$ . This relationship will be investigated further below.

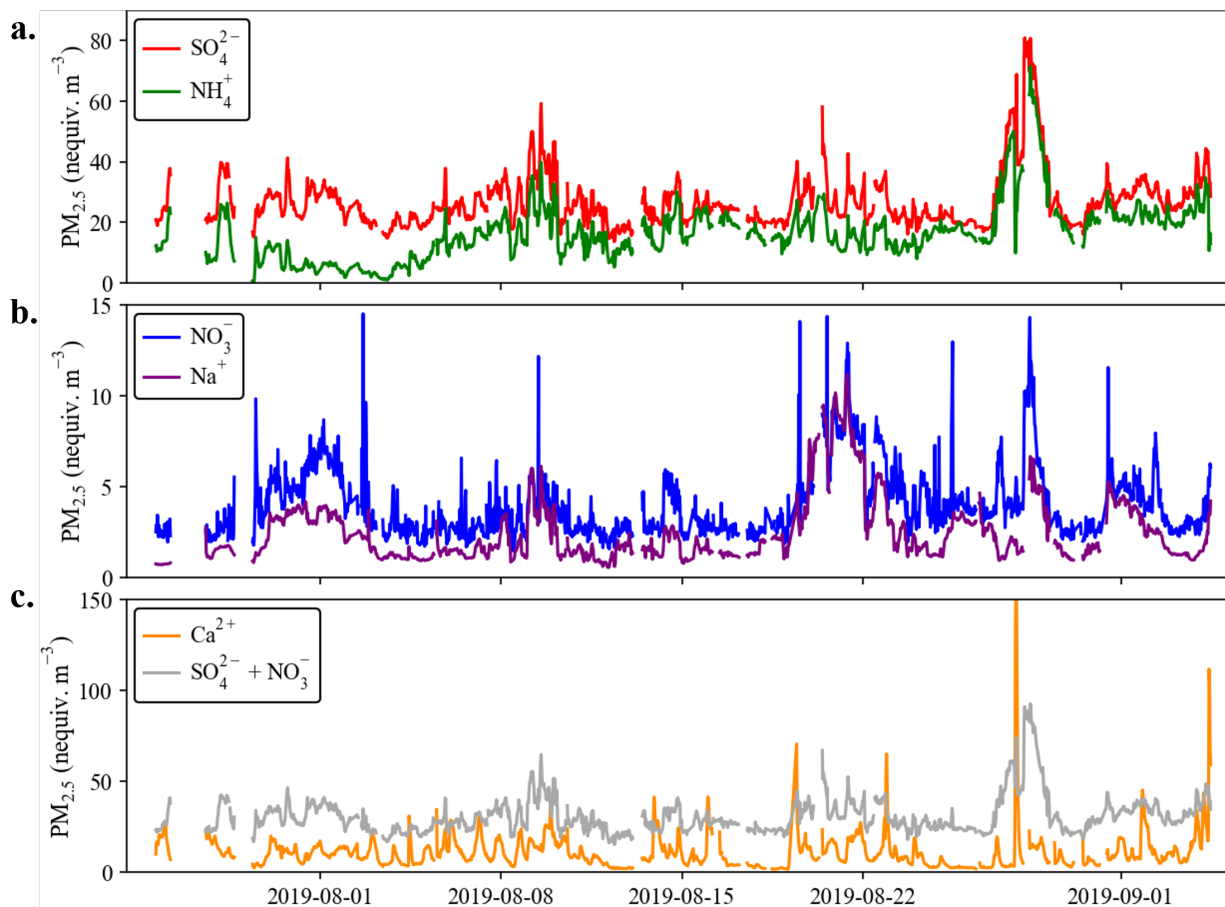


**Figure 3.3:** PILS-IC species ammonium, sulfate, nitrate, and sodium are shown as nano equivalents per meter squared (nequiv. m<sup>-3</sup>). (a.) Sulfate is shown in red and ammonium in green, (b.) shows nitrate in blue and sodium in purple, and (c.) shows calcium in orange and the sum of sulfate and nitrate in grey.

A timeline of the sum of sulfate and nitrate is plotted with Ca<sup>2+</sup> concentrations in Figure 3.3 (c.). There are several short-term Ca<sup>2+</sup> concentration spikes, likely associated with local or regional dust events, which exceed 50 nequiv. m<sup>-3</sup>. A linear regression of Ca<sup>2+</sup> vs the sum of SO<sub>4</sub><sup>2-</sup> and NO<sub>3</sub><sup>-</sup> yields a slope of 1.6 and  $R^2$  of 0.11. The short-term spike values were filtered from the data set by removing Ca<sup>2+</sup> concentrations greater than one standard deviation larger than the mean (avg. 11.3 and standard deviation 10.7 nequiv m<sup>-3</sup>). This removed 135 data points. The resulting linear regression of the filtered data set had a slope of 2.7 and  $R^2$  of 0.14. The low  $R^2$  value for the filtered and unfiltered data sets indicates that there is a large amount of variability in the Ca<sup>2+</sup> concentration, unrelated to either SO<sub>4</sub><sup>2-</sup> or NO<sub>3</sub><sup>-</sup>. This could indicate a large presence of

$\text{CaCO}_3$ , from local dolomite erosion and dust formation. The correlation might also be degraded by the presence of sulfate produced from reaction of anthropogenically emitted  $\text{SO}_2$ .

The “excess” sulfate, shown in Figure 3.3 (a.) is further illustrated in Figure 3.4.  $\text{SO}_4^{2-}$  equivalent concentrations are plotted against the corresponding  $\text{NH}_4^+$  equivalent concentration for each PILS-IC data point. All observations are above the one-to-one line with a slope of 1.4 for a least squares best fit line. This indicates that there is not enough particle ammonium to fully neutralize the observed sulfate. Given the excess ammonia present in the gas phase, the lack of sulfate neutralization by ammonium could reflect the presence of gypsum dust in the aerosol or the presence of calcium carbonate dust that has reacted with sulfuric acid.

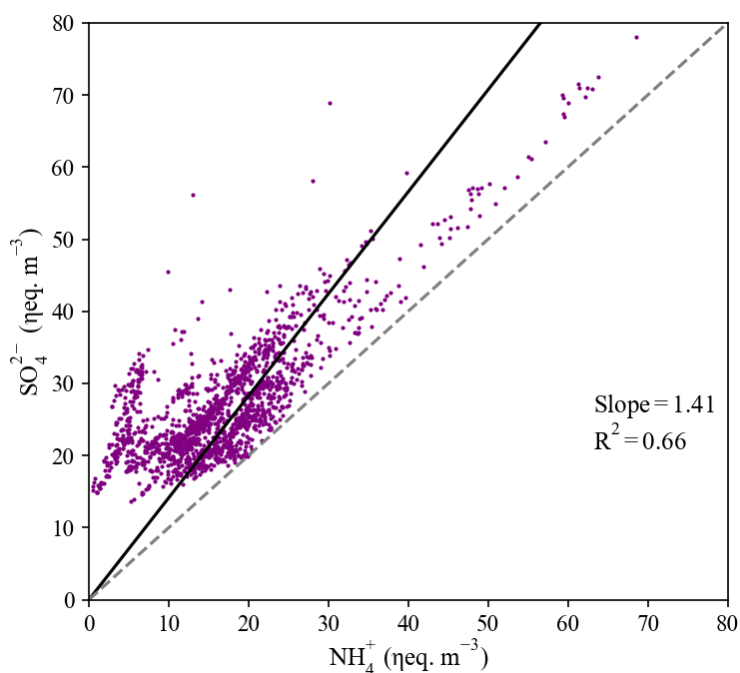


**Figure 3.4:** Fine particle sulfate is plotted against ammonium, both given in  $\eta\text{equiv. m}^{-3}$ . The dotted grey line shows a slope of one. A simple linear regression was fitted to the purple data points and yielded a slope of 1.41 and  $R^2$  of 0.66. The best fit line was forced through the origin and is shown in black.

The importance of ammonium nitrate formation can be assessed using a minimum useful correlation. Given that sulfate and ammonium are correlated, a minimum correlation between nitrate

and ammonium can be calculated using the equation below.

$$|r(\text{NO}_3^-, \text{NH}_4^+)|_{\text{minimum useful}} > |r(\text{SO}_4^{2-}, \text{NH}_4^+)| * |r(\text{SO}_4^{2-}, \text{NO}_3^-)| \quad (3.1)$$

The equation states that in order for  $\text{NO}_3^-$  to helpfully explain the variation in  $\text{NH}_4^+$ , the correlation needs to be larger than the correlation between  $\text{SO}_4^{2-}$  and  $\text{NH}_4^+$  and the correlation between  $\text{SO}_4^{2-}$  and  $\text{NO}_3^-$ . In Figure 3.5  $\text{SO}_4^{2-}$  and  $\text{NO}_3^-$  are each plotted against  $\text{NH}_4^+$ . Their correlations are 0.66 and 0.05 respectively. The calculated minimum useful correlation for  $\text{NO}_3^-$  and  $\text{NH}_4^+$  is 0.13, which is larger than 0.05. Therefore including  $\text{NO}_3^-$  in the correlation does not explain more of the variation in  $\text{NH}_4^+$  than  $\text{SO}_4^{2-}$  alone. This supports the hypothesis that the  $\text{NO}_3^-$  measured during this campaign is not present as  $\text{NH}_4^+\text{NO}_3^-$ .

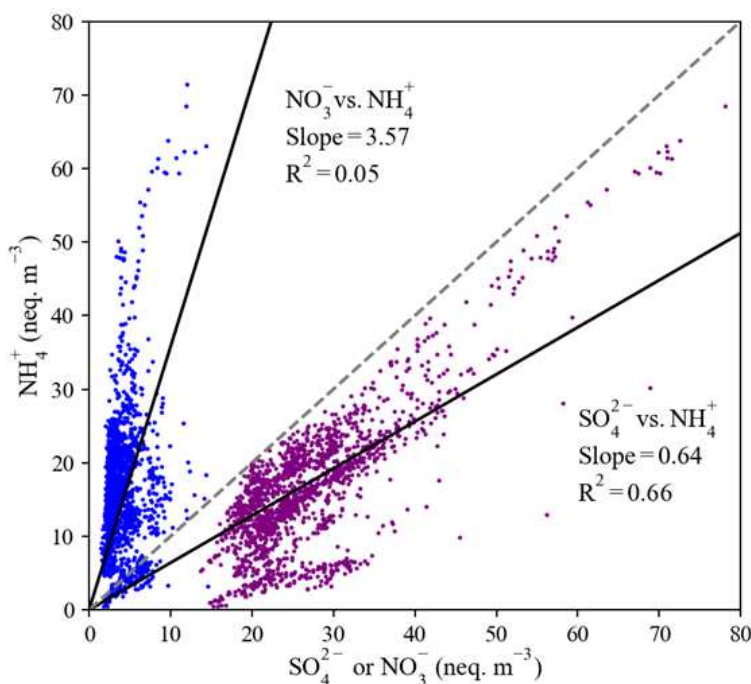


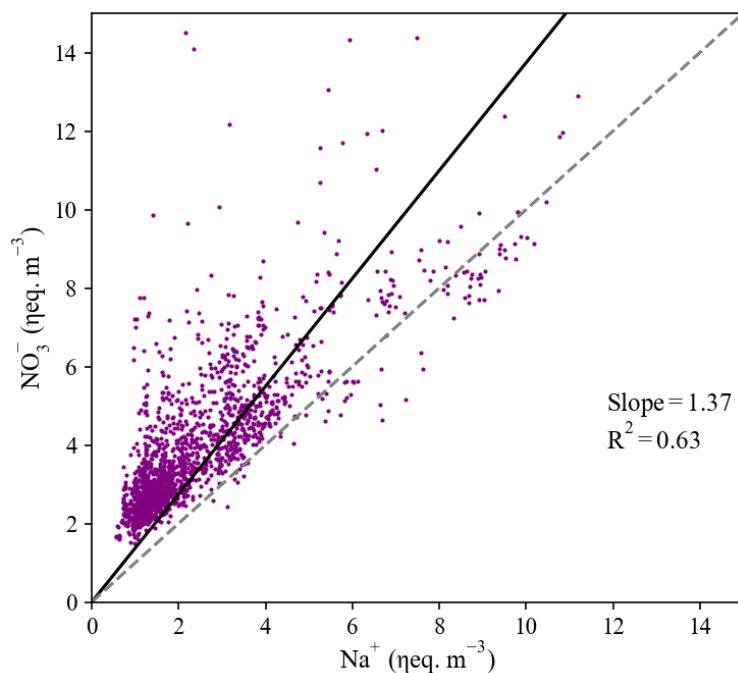
**Figure 3.5:** Fine particle  $\text{SO}_4^{2-}$  and nitrate are both plotted against ammonium in nequiv.  $\text{m}^{-3}$ . Each has an ordinary least squares linear regression plotted in black. The corresponding slope and  $R^2$  values are next to the fits.

Given that this intensive was conducted in summertime with high temperatures (avg. 28 C) and low RH (avg. 36%) the formation of ammonium nitrate is not expected thermodynamically. Assuming that ammonium nitrate is not a contributor to the aerosol composition, given the hot dry conditions, much, but not all, of the measured  $\text{NO}_3^-$  can be explained by reaction between sea salt and nitric acid. Additional  $\text{NO}_3^-$  could be present due to the reaction between calcium carbonate and nitric acid (Equation 1.1) or its precursors, as discussed above. The reactions of nitric acid with sea salt and soil dust can compete and account for formation of supermicron, between 1 and 2.5  $\mu\text{m}$ ,  $\text{NO}_3^-$  aerosol of differing composition.  $\text{CaCO}_3$  and  $\text{HNO}_3$  readily react with each other at low RH values [Krueger et al., 2003], like those seen in CAVE, and this reaction has been found to be important for  $\text{NO}_3^-$  aerosol formation [Fairlie et al., 2010; Jordan et al., 2003]. The calcium carbonate could be from dolomite (or limestone) erosion and dust formation. There are significant dolomite deposits in the Permian Basin [Johnson, 1997]. From the URG denuder data (see Figure 3.2), we see that there is significant nitric acid present in the gas phase on all days during the study period, supporting the likelihood of its reaction with available sea salt or soil dust aerosol as a source of aerosol  $\text{NO}_3^-$ .

Previous research has found the formation of supermicron  $\text{NO}_3^-$  aerosol from sea salt and soil dust to be important in a number of national parks. During the Big Bend Regional Aerosol and Visibility Observational (BRAVO) in west Texas, researchers found that  $\text{NO}_3^-$  was mostly associated with sea salt particle  $\text{Na}^+$ , but that the formation of calcium nitrate was also important on several days [Lee et al., 2004]. Malm et al. [2005] found that in Yosemite National Park nitrate was often present in supermicron aerosol as a result of reaction with transported sea salt. Following these two studies, the coarse mode nitrate was characterized at a number of IMPROVE monitoring sites by Lee et al. [2008]. Of the five sites characterized, four had contributions from supermicron nitrate: Grand Canyon National Park, Great Smokey Mountains National Park, Brigantine National Wildlife Refuge, and San Geronio Wilderness Area. At the Southern California San Geronio site, nitrate during spring was primarily present as submicron ammonium nitrate, while during hotter summer conditions reacted sea salt and reacted soil dust together comprised about one-third

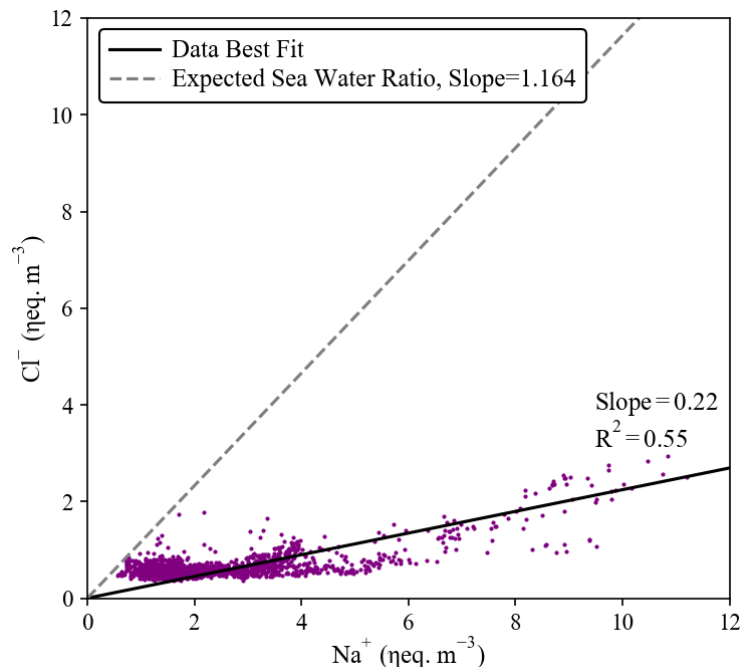
of total particulate nitrate. Coarse mode nitrate formation from soil and sea salt accounted for the majority of particle nitrate in Grand Canyon and the Great Smokey Mountains [Lee et al., 2008]. The relative importance of ammonium nitrate vs. sodium and calcium nitrate was observed to depend on the availability of ammonia, sea salt, and soil dust as well as environmental conditions (temperature and RH) that influence the formation of ammonium nitrate.

The relationship between nitrate and sodium shown in Figure 3.3 (b.) is further investigated in Figure 3.6. Nitrate is plotted directly against sodium, to assess the importance of reaction of sea salt with nitric acid or its precursors (see Equation 1.1). The reaction between nitric acid and sea salt drives chloride out of the aerosol phase by forming gaseous hydrochloric acid. Nitrate in Figure 3.6 is nearly always in excess over  $\text{Na}^+$ , although there are some points below the one-to-one line. These points move above the line if the chloride concentration is added to the y-axis nitrate value suggesting that the combined levels of nitrate and chloride are sufficient to explain any  $\text{Na}^+$  coming from sea salt emissions.



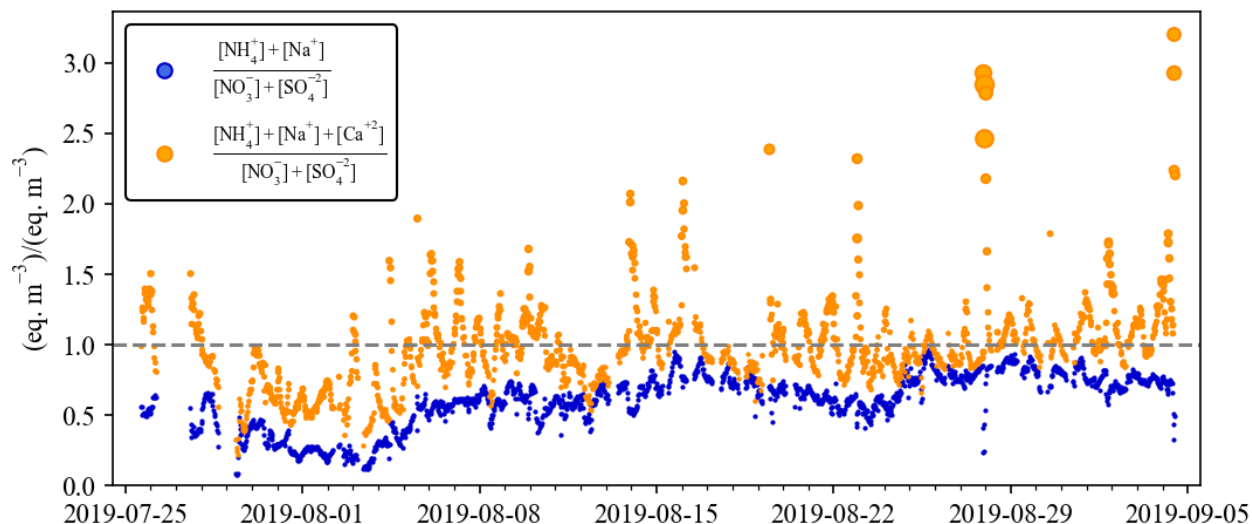
**Figure 3.6:** Fine particle nitrate is plotted against sodium, both given in  $\text{nequiv. m}^{-3}$ . The dotted grey line shows a slope of one. A simple linear regression was fitted to the purple data points and yielded a slope of 1.37 and  $R^2$  of 0.63. The best fit line was forced through the origin and is shown in black.

Further comparison of the measured  $\text{PM}_{2.5} \text{Cl}^-$  to  $\text{Na}^+$  ratios in Figure 3.7 shows that they are consistently below the expected sea salt ratio of 1.16, with an average ratio of 0.34, again suggesting hydrochloric acid displacement from the aerosol by reaction with nitric acid.



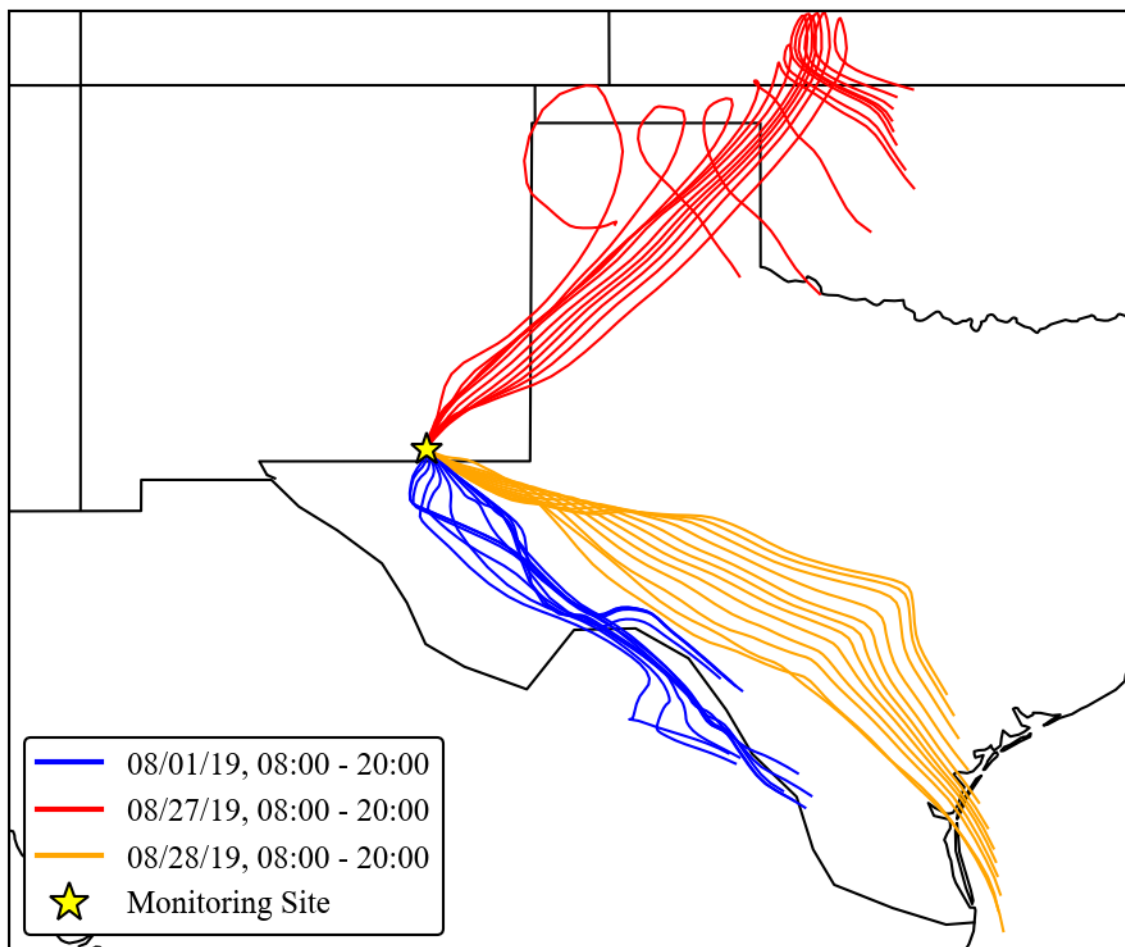
**Figure 3.7:** Fine particle chloride is plotted against sodium, both given in nequiv.  $\text{m}^{-3}$ . The dotted grey line shows the expected ratio of chloride to sodium from sea water (1.164). A simple linear regression was fitted to the concentration data points and yielded a slope of 0.22 and  $R^2$  of 0.55. The best fit line was forced through the origin and is shown in black.

Figure 3.8 looks at the ratio of cations and anions measured by the PILS-IC system more holistically. The ratio of  $\text{Na}^+$  plus ammonium to  $\text{SO}_4^{2-}$  plus nitrate always falls below a value of 1.0, indicating an excess of the anion species. The presence of substantial gas phase ammonia means it is unlikely that the aerosol is acidic enough for  $\text{H}^+$  to balance the excess anion levels. Adding  $\text{Ca}^{2+}$  to the (cation) numerator of the ratio changes the story significantly. Now many of the observations exhibit a cation/anion ratio close to 1.0, consistent with charge balance. There does appear to be a period of acidic aerosol from 07/29/2019 to 08/03/2019 and there are several shorter periods where the cation/anion ratio climbs toward 2 or higher. The values where the ratio is highest are associated with high  $\text{Ca}^{2+}$  concentrations. The deficiency in measured anion species likely represents the presence of considerable carbonate in this dust-rich aerosol. As mentioned earlier, carbonate is not detected by the PILS-IC system. Overall, Figure 8 indicates that  $\text{Ca}^{2+}$  plays an important role in the  $\text{PM}_{2.5}$  aerosol ion balance.



**Figure 3.8:** The ratio of anion and cation species measured by the PILS-IC is plotted in  $\text{eq. m}^{-3}$ . The dotted grey line shows a ratio of unity. The blue points include ammonium and sodium for the cations, and the orange points add calcium to the cation species. The radius of the cation point size changes proportionally with calcium concentration.

Transport during different aerosol composition periods was considered using HYSPLIT trajectory analysis. The trajectories were run for 48 hours. A set of daytime (08:00 to 20:00) trajectories is shown in Figure 3.9 for the period of acidic aerosol on 08/01/19 (Figure 3.8), the period of highest gaseous ammonia on 08/27/19 (Figure 3.2), and the largest total  $\text{PM}_{2.5}$  peak from the PILS-IC on 08/28/19 (Figure 3.1). Only the daytime trajectories are considered here due to increased variability in transport patterns overnight. Transport on 08/27/19 comes from the northeast and passes near two major coal-fired power plants shown in Figure 1.2, which could explain the observed increase in sulfur compounds. This region also includes the largest agricultural production in the area based on the 2017 USDA Census of Agriculture (map in Appendix A.), consistent with the elevated ammonia and ammonium in the URG data. Transport on 08/28/19 comes from the southeast over the largest concentration of O/G wells in the region and connects down to the Gulf of Mexico. This 48-hour transport pattern illustrates the importance of the Gulf of Mexico as a sea salt source region to support the reaction with nitric acid discussed above. The period of acidic aerosol on 08/01/19 also features transport from the southeast but shifted further south and moving more slowly than the 8/28 transport pattern. The air mass sampled at CAVE on this data has more



**Figure 3.9:** 48-hour HYSPLIT Back Trajectories are shown for three different transport patterns during the study. The dates were selected based on aerosol composition. 12 daytime (08:00-20:00) back trajectories of 48-hour duration are plotted for each date.

limited ammonia and ammonium, consistent with the more acidic aerosol and the lack of major agricultural emissions in the upwind region. The transport patterns observed in the study will be considered in more detail in section 3.4.

## 3.2 Mass Closure and Visibility Impacts

The sum of mass concentrations of the higher time resolution speciated  $PM_{2.5}$  measurements (PILS-IC species, BC, and WSOC multiplied by a factor of 1.8 to account for species beyond carbon in the organic aerosol [Prenni et al., 2019]) did not reach full mass closure when compared with the total  $PM_{2.5}$  mass measured by the TEOM (see Figure 3.10). This is not surprising given

the regional importance of insoluble or unquantified components of airborne mineral dust. The mean difference between the speciated and total  $PM_{2.5}$  in the high time resolution dataset was 43 percent, indicating that the non-water-soluble and unmeasured (e.g., carbonate) fine aerosol species make up a significant portion of the total fine aerosol mass.

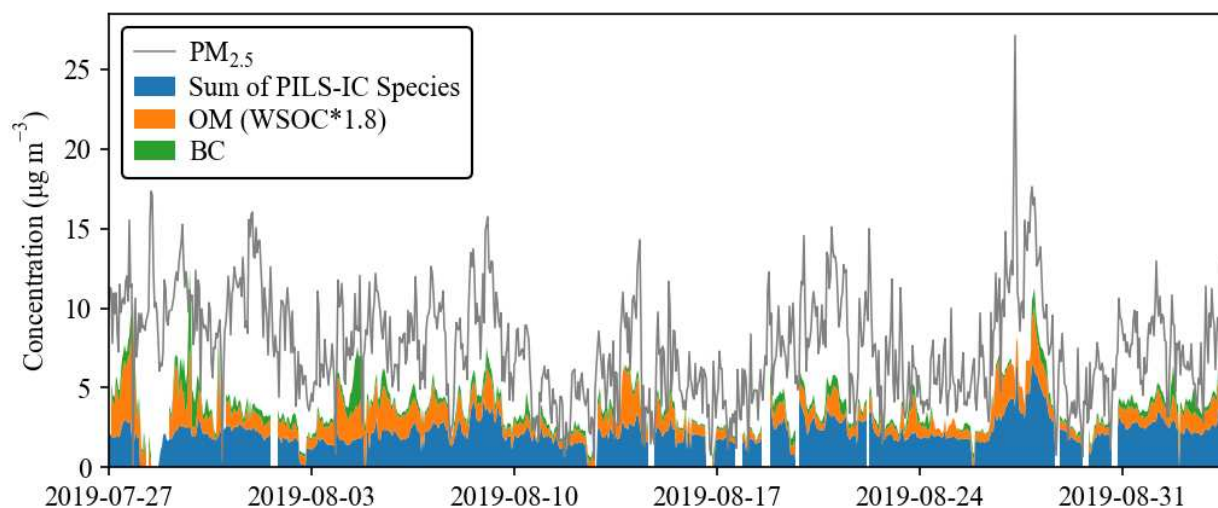


**Figure 3.10:** Speciated  $PM_{2.5}$  measurements are shown as a sum, with the total  $PM_{2.5}$  measured by the TEOM shown as a grey line. The sum of all species measured by the PILS-IC is shown in blue. Organic matter is shown in orange, estimated at 1.8 times the WSOC. Black carbon is shown in green from the Aethalometer at 880 nm.

To better account for the aerosol mineral components the lower time resolution IMPROVE data set was examined. IMPROVE measures elemental species by XRF, which captures the non-water-soluble mineral dust fraction of the  $PM_{2.5}$  aerosol, as well as OC (vs. the water soluble WSOC fraction in the PILS). The IMPROVE total  $PM_{2.5}$  reconstructed from measured species concentrations is compared to the total  $PM_{2.5}$  mass measured by the TEOM in Figure 3.11. To be directly compared, the TEOM measurements were averaged across 24 hours and filtered to only the days that the IMPROVE module took measurements. A slope of 0.9 for a best fit least-squares regression line with an  $R^2$  of 0.79 indicates that the regression captures the trend in the data well and that the reconstructed and measured  $PM_{2.5}$  mass are in close agreement. Most of the comparison points are centered closely around the 1:1 line, with just one point of much lower

reconstructed IMPROVE PM<sub>2.5</sub> mass pulling the fit slope farther below one. Excluding that point yields a slope of 0.93 for the comparison, with an  $R^2$  of 0.94.

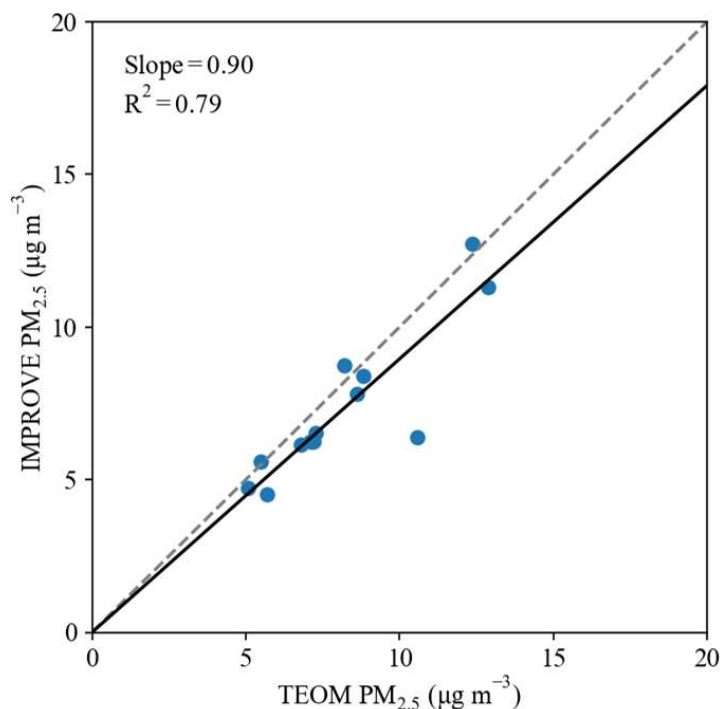


**Figure 3.11:** IMPROVE PM<sub>2.5</sub> is plotted against TEOM PM<sub>2.5</sub> in  $\mu\text{g m}^{-3}$ . The TEOM data set was resampled to a 24-hour mean and plotted for only the points with an IMPROVE. A least-squares linear regression shown in black was fitted to the data and forced through zero measurement. The grey dotted line is the 1:1 line, or  $y=x$ .

The IMPROVE mass reconstruction assumes that nitrate is present as ammonium nitrate and  $\text{SO}_4^{2-}$  is present as ammonium sulfate. Although the PILS speciated data suggest that the nitrate is likely present as a mix of sodium and calcium nitrate while the  $\text{SO}_4^{2-}$  may be partly present in combination with  $\text{Ca}^{2+}$ , this does not greatly impact the mass closure since the nitrate concentrations are fairly low and the equivalent masses of  $\text{NH}_4^+$ ,  $\text{Na}^+$ , and  $\text{Ca}^{2+}$  are similar at 18, 22, and 20 g per mole of charge, respectively. Mass closure in Figure 3.12 (a.) has significant contributions from  $\text{SO}_4^{2-}$ , OM ( $\text{OC} \cdot 1.8$  [Prenni et al., 2019]), and fine soil. Fine soil is calculated in the IMPROVE data set by Equation 1.4. The reconstructed mass contains a significant contribution (average of 29.6% and maximum of 64.9%) from fine soil. This large contribution is consistent

with the significant shortfall (average of 43%) in mass closure for the higher time resolution study aerosol measurements discussed above.

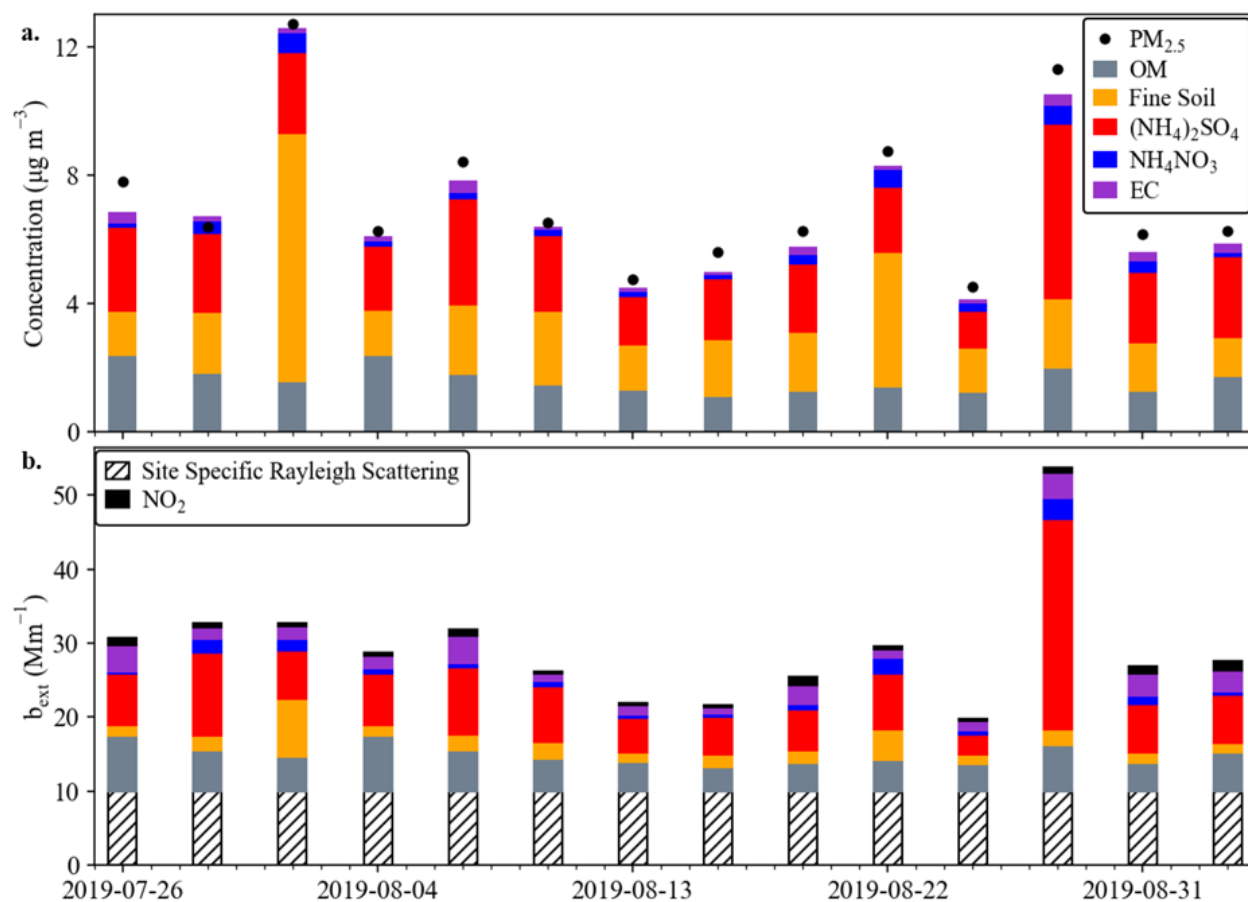


**Figure 3.12:** IMPROVE mass closure is plotted in the upper panel, as the sum of OM, fine soil, ammonium sulfate, ammonium nitrate, and elemental carbon. The total  $\text{PM}_{2.5}$  by mass is also shown by the black dots. (b.) The contribution to light extinction from each species plotted in (a.) as calculated using the second IMPROVE algorithm for light extinction. Site specific Rayleigh Scattering ( $10 \text{ Mm}^{-1}$ ) is included in addition to fine particle species.  $\text{NO}_2$  (g) light extinction is calculated using the second IMPROVE algorithm and a resampled daily mean of the measured  $\text{NO}_2$ .

Figure 3.12 (b.) shows the calculated light extinction from each of the species (OM, fine soil, ammonium sulfate, ammonium nitrate, EC, and background Rayleigh Scattering). These values were calculated using the second IMPROVE algorithm [Pitchford et al., 2007; Prenni et al., 2019]. This light extinction calculation again assumes that nitrate is present as ammonium nitrate. Light extinction is influenced by particle refractive index, assumed size distribution, and hygroscopicity,

which differ for ammonium nitrate vs. sodium or calcium nitrate. In the end, however, the 24-hour light extinction from nitrate is a small contributor relative to other species.  $\text{NO}_2$  (g) high-time resolution data was resampled to a 24-hr value, and used to calculate  $\text{NO}_2$  light extinction. The IMPROVE  $\text{NO}_2$  data was below the limit of detection for all days except for one during the CarCavAQS project. Agreement between the high-time resolution  $\text{NO}_2$  data and IMPROVE  $\text{NO}_2$  data on that day was very poor, differing by greater than an order of magnitude. Due to the rigorous QA/QC measures used for the the high-time resolution  $\text{NO}_x$  measurements, these data were used for this analysis.

The reconstructed particle light extinction for IMPROVE sample days is typically dominated by  $\text{SO}_4^{2-}$ , with a mean fractional contribution of 42% and a range from 19% to 69% during the study. Extinction by organic matter, EC, fine soil, and ammonium nitrate averaged 29%, 14%, 10%, and 4.9%, respectively. OM was the largest contributor to particle light extinction on 5 days (July 14, August 4, 13, and 25, and September 24). Fine soil was the largest contributor on August 1st.

To better understand higher short-term variability in aerosol species' contributions to light extinction, the second IMPROVE algorithm was also applied to our higher time resolution composition data. To do this several assumptions were needed. Some of these assumptions impact the absolute accuracy of the estimated extinction, but the goal here is to ascertain the variability in light extinction on short timescales and whether short term concentration excursions lead to species other than  $\text{SO}_4^{2-}$ , OM, or fine soil dominating the extinction budget at hourly timescales.  $\text{SO}_4^{2-}$  and nitrate were again assumed to be present as ammonium sulfate and ammonium nitrate, consistent with the IMPROVE light extinction calculations above.

Major species measured directly by IMPROVE and by the PILS ( $\text{SO}_4^{2-}$ , nitrate, calcium, and sodium) agreed reasonably well, differing by less than 25% on average.  $\text{SO}_4^{2-}$  (Figure 3.13 (a.)), nitrate (Figure 3.13 (b.)), sodium (Figure 3.13 (c.)), and calcium (Figure 3.13 (d.)) differed on average by 19%, 20%, 22%, and 23% respectively. Plots of these comparisons are shown in Figure 3.13. Each plot has a least squares linear regression, forced through zero measurement and a 1:1

line shown in dashed grey. For  $\text{SO}_4^{2-}$ , sodium, and calcium, the PILS data is consistently lower than the corresponding IMPROVE values. This is not surprising for calcium and sodium, which may include insoluble mineral components. As such, these components are considered a lower bound in the light extinction calculation. The nitrate data, has a slope of 0.98 and a  $R^2$  of 0.9, indicating that the PILS  $\text{NO}_3^-$  data represents the IMPROVE  $\text{NO}_3^-$  well.

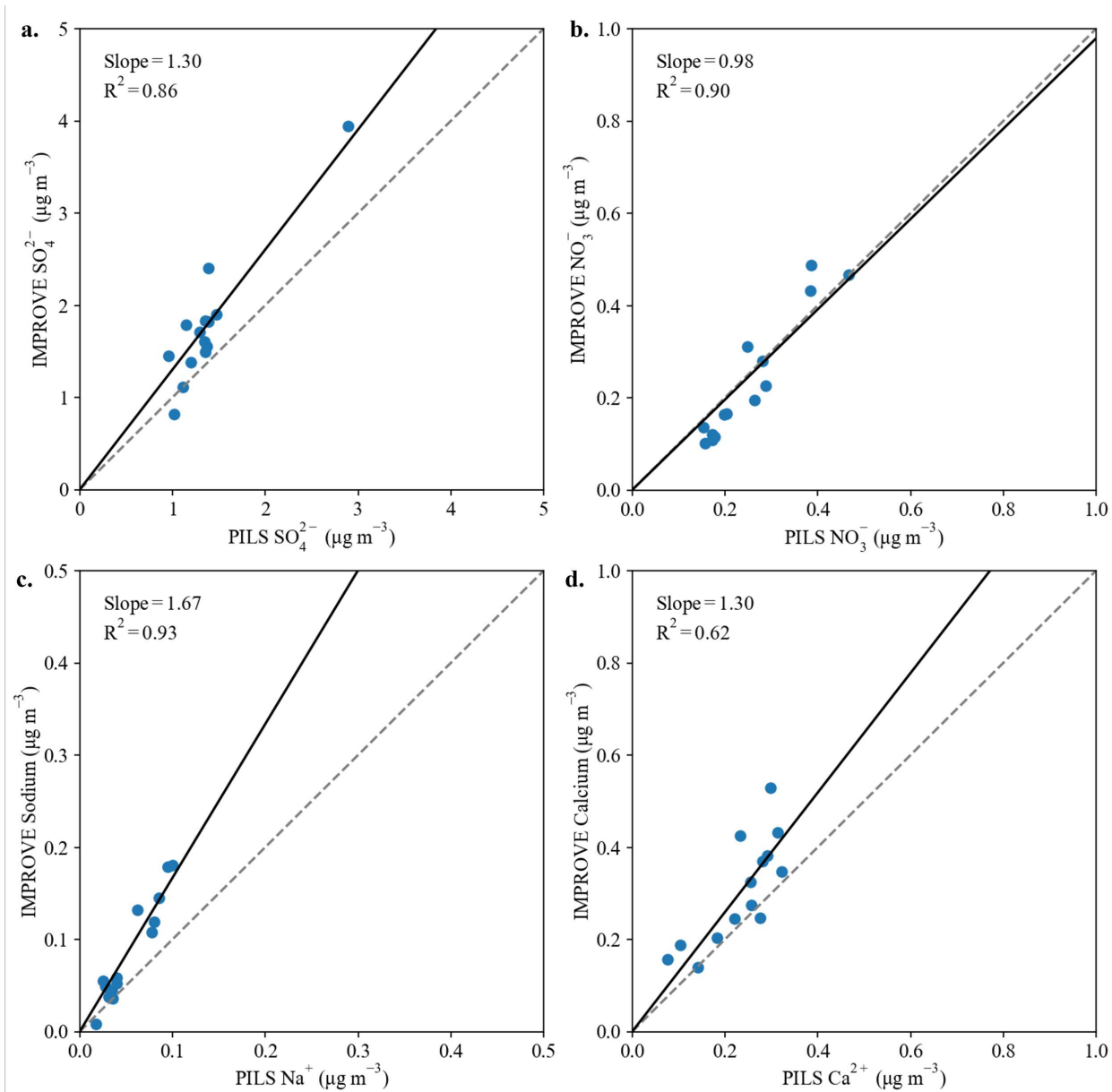


**Figure 3.13:** Major  $PM_{2.5}$  species are plotted from the IMPROVE and PILS-IC data sets. PILS-IC species were resampled to a daily mean and plotted for the days with an IMPROVE measurement. A least-squares linear regression was fitted to each set of points and forced through zero measurement. (a.)  $SO_4^{2-}$  is compared between the data sets. IMPROVE  $SO_4^{2-}$  was calculated directly from the given  $(NH_4)SO_4$ . (b.)  $NO_3^-$  is compared between the data sets. IMPROVE  $NO_3^-$  was calculated directly from the given  $NH_4NO_3$ . (c.) Sodium is compared between the data sets. (d.) Calcium is compared between the data sets.

To estimate fine soil, study average IMPROVE concentrations were used for each elemental species in Equation 1.4, except for calcium. Calcium exhibited the largest range of fractional contribution to IMPROVE fine soil by a significant margin (see Table 3.1) and was the only species

in the IMPROVE soil equation measured in the PILS. The PILS, however, measured water soluble  $\text{Ca}^{2+}$  ion, which represents a fraction of the elemental Ca present and measured by XRF in the IMPROVE samples. A comparison of PILS  $\text{Ca}^{2+}$  vs. IMPROVE Ca revealed that water soluble  $\text{Ca}^{2+}$  comprised an average of 78% of elemental Ca, with a range of 48% to 100%, indicating that our substitution of  $\text{Ca}^{2+}$  for Ca in the IMPROVE soil equation represents a lower bound on that component of fine soil.

**Table 3.1:** The fractional contribution to total fine soil for the IMPROVE data set is shown for each of the elemental constituents from Equation 1.4. The range of their fractional daily contributions is also calculated over the data set.

Element	Average Fractional Contribution to Fine Soil	Range of Fractional Contribution
Al	0.17	0.11 – 0.22
Si	0.46	0.35 – 0.53
Ca	0.25	0.09 – 0.45
Fe	0.11	0.08 – 0.14
Ti	0.01	0.01 – 0.02

PILS WSOC was used as an estimate for OC and converted to OM using the second IMPROVE algorithm scale factor (1.8) [Prenni et al., 2019]. A comparison of IMPROVE OC vs. PILS WSOC showed good correlation ( $R^2$  of 0.64) with a slope of 1.09 (see Figure 3.14), so we are estimating a lower bound for the OC contribution to light extinction. The water-soluble fraction of total OC may be more variable at higher time resolution, however, in the daily average, it typically accounts for most of the total OC. One data point in Figure 3.14 where WSOC/OC exceeds 1 is physically implausible.

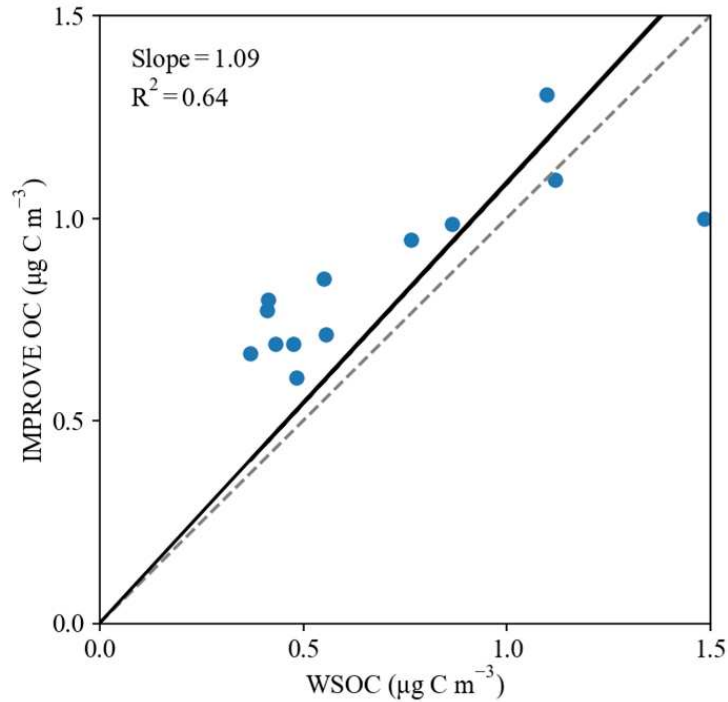


**Figure 3.14:** IMPROVE OC is plotted against the PILS-WSOC measurement. WSOC was resampled to a daily average and plotted for only the days with IMPROVE measurements taken. A linear regression was fitted to the data and is shown in black. The slope of the least-squares linear regression is 1.09 and it has an  $R^2$  of 0.64. The grey dashed line has a slope of 1.

Utilizing these assumptions, averaging high time resolution concentration measurements to one hour, and making use of hourly meteorological data from the National Park Service at CAVE, particle light extinction was calculated at hourly time frequency (Figure 3.15). The maximum  $b_{\text{ext}}$  values, likely lower bounds as discussed in the assumptions above, are between  $60$  and  $90 \text{ Mm}^{-1}$  vs. a daily maximum of  $54 \text{ Mm}^{-1}$  determined from the 24-hour IMPROVE measurements.

The  $b_{\text{ext}}$  peaks represented by points “a” and “c” in Figure 3.15 highlight maximum contributions to light extinction by different species. Point “a” has a majority contribution from BC. It is important to note that point “a” does not correspond to the BC maximum ( $16 \mu\text{g m}^{-3}$ ). That maximum value, which was missing other data sets due to a power outage, corresponds to the first peak in the light extinction plot. This peak is not discussed due to the data gaps for certain data sets. The  $\text{NO}/\text{NO}_x$  ratio at this time is not elevated (ratio of 0.22) compared to other time periods (daytime avg 0.2), likely ruling out a very local combustion source (i.e., a passing truck near the inlet), as

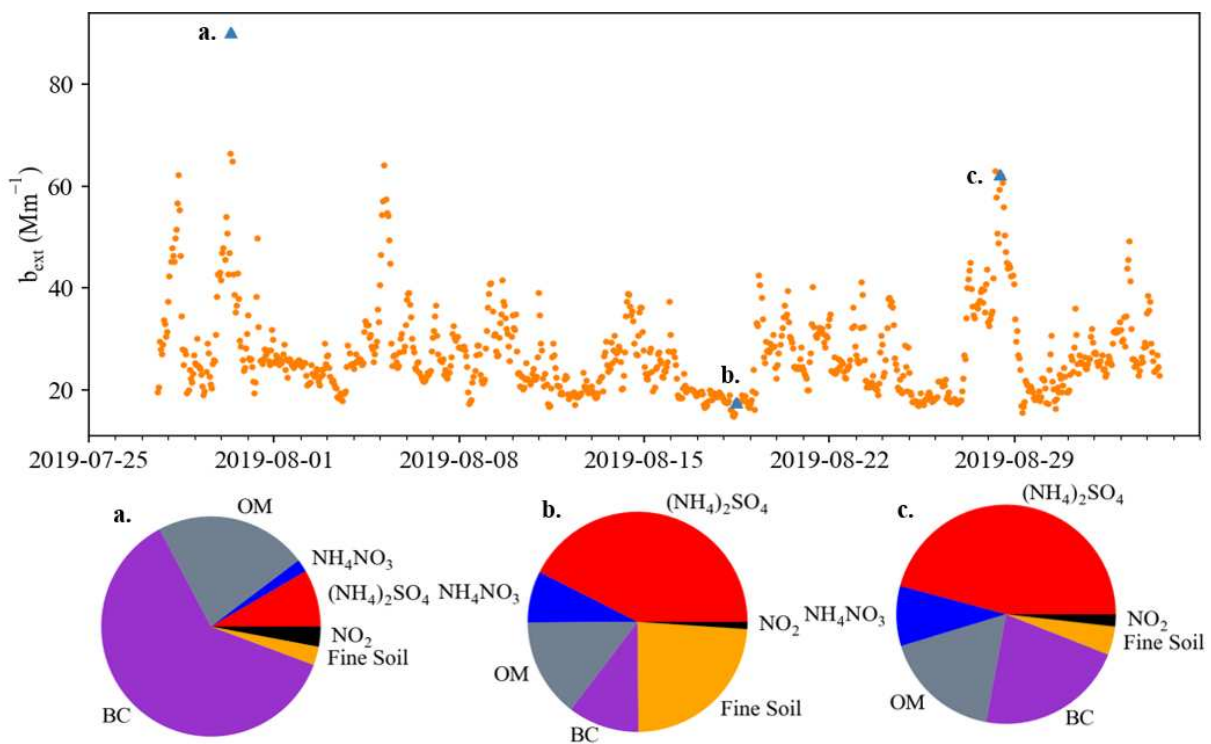


**Figure 3.15:** PM<sub>2.5</sub> reconstructed light extinction is shown above. The second IMPROVE equation was applied to our higher time resolution composition data (PILS-IC, PILS-WSOC, Aethalometer BC and NO<sub>2</sub>). These values include the Rayleigh background contribution (10 Mm<sup>-1</sup>). The fractional light extinction contributions, excluding the site specific Rayleigh scattering, of the different species are shown for three data points (shown as blue triangles). Extinction peaks highlighting maximum contributions are represented by points a and c (30 July 2019 09:00 MST and 28 August 2019 12:00 MST). Point b represents a low light extinction period on 18 August 2019 12:00 MST.

does the duration of this extinction event across multiple hours. A high methane mixing ratio (2.4 ppmv) coinciding with this light extinction peak suggests O/G activity, likely flaring or diesel engine emissions, as a source of the BC that dominates this 90 Mm<sup>-1</sup> hourly extinction episode. Both points “b” and “c”, with low and high hourly  $b_{\text{ext}}$  respectively, have the largest extinction contributions from  $\text{SO}_4^{2-}$ , similar to the typical pattern we saw at daily time resolution using the IMPROVE data. Both high extinction points (a and c) have corresponding NOAA HYSPLIT back-trajectories which come from the south-east sector, a region of intense O/G development and production. The high variability in hourly light extinction values and the different aerosol compositions during peak extinction episodes point to the importance of high time resolution measurements to better characterize peaks in visibility impairment in the park and the activities responsible for those episodes.

### 3.3 HYSPLIT Residence Time Analysis

Incremental probability (IP) distributions for the residence time analyses conducted for major species and associated light extinction are presented in Figure 3.16. Red grid cells indicate that the air mass was more likely to have passed through that grid cell on a high concentration/extinction trajectory (top 10% of parameter values) than during the full set of study back-trajectories. Blue grid cells indicate that passage of a trajectory through that cell was more likely during the full trajectory set than on a high concentration/extinction trajectory. High concentration periods of  $\text{SO}_4^{2-}$ , ammonium and WSOC show prevailing directionality from the SE and from the NE. The high concentration trajectory similarity for  $\text{SO}_4^{2-}$  and ammonium reflects the tight association between those aerosol components. The SE is associated with the largest number of nearby oil and gas well. The elevated  $\text{SO}_4^{2-}$  could be tied to the two coal fire power plants to the NE, shown in Figure 1.2. Coal burning is associated with large emissions of  $\text{SO}_2$ , a gaseous precursor to  $\text{SO}_4^{2-}$  aerosol [U.S. EIA, 2022b]. The NE also corresponds to the largest number of nearby agriculture activity by production value, based on the USDA Census of Agriculture [2017]. A map of the agriculture in the region can be found in the supplementary materials.

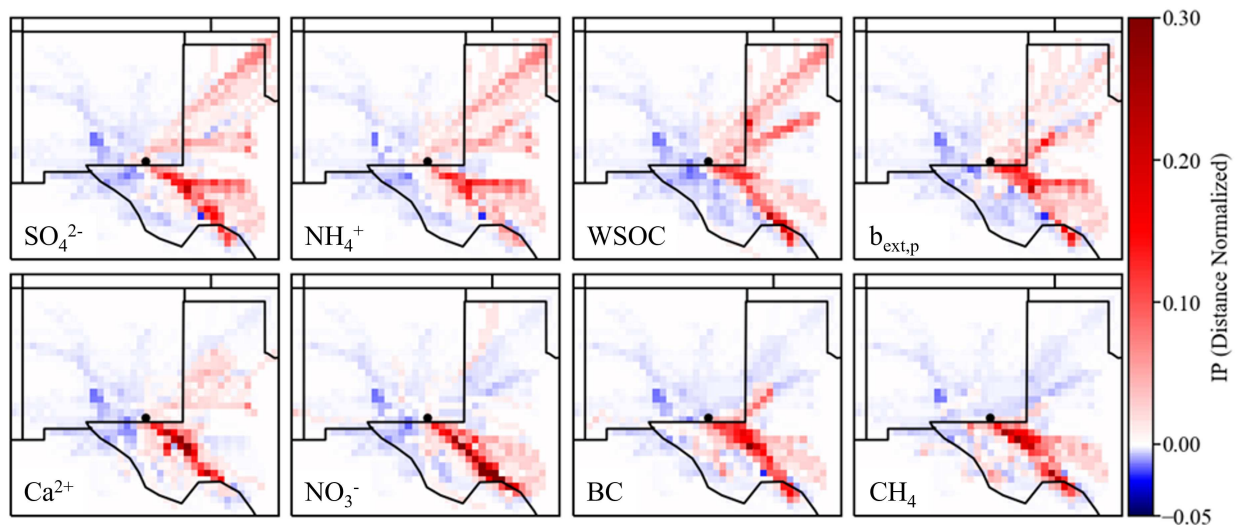


**Figure 3.16:** Incremental probability distributions are plotted for 7 species measured directly during the field campaign: sulfate, ammonium, water-soluble organic carbon, calcium, nitrate, black carbon, and methane and 1 calculate value: light extinction ( $b_{ext}$ ). The IPs are based on 24-hour back trajectories and are distance normalized. This is done by multiplying each grid cell value by the distance from the origin site, shown as a black dot. The grid cell resolution is 0.25 degrees square.

The light extinction plot ( $b_{ext}$ ) shows the most haze-impacted periods more strongly associated with transport from the SE, although some influence from the NE remains. The bottom row of species in the figure ( $Ca^{2+}$ ,  $NO_3^-$ , BC, and  $CH_4$ ) shows most high concentration measurement periods associated with transport from the SE. The SE sector corresponds with the highest concentration of nearby O/G activity, a likely source of  $NO_3^-$  precursor  $NO_x$ , BC, and  $CH_4$ . The SE sector also corresponds with Permian Basin limestone and gypsum deposits, a likely source of soil dust rich in calcium carbonate and calcium  $SO_4^{2-}$ .

# Chapter 4

## Summary and Future Research Directions

### 4.1 Summary

Unconventional oil and natural gas development is driving oil and natural gas production increases in the U.S. [U.S. EIA, 2021a]. Previous studies have focused predominately on greenhouse gas emissions from O/G or on emission contributions to ozone formation. Relatively few studies have focused on oil and gas impacts on PM<sub>2.5</sub> and haze formation. The CarCavAQS study in Carlsbad Caverns National Park provided novel and important insight into the composition and likely sources of particulate matter in the region.

PM<sub>2.5</sub> mass ranged up to 31.8  $\mu\text{g m}^{-3}$ , with an average of 7.67  $\mu\text{g m}^{-3}$ . The main contributions came from ammonium sulfate, sodium nitrate, fine soil, organic carbon, and black carbon. The mean difference between the sum of hourly time-resolution speciated species and total PM<sub>2.5</sub> mass was 43%. Speciated PM<sub>2.5</sub> had good mass closure from the IMPROVE 24-hour time-resolution data set. On average, the IMPROVE reconstructed mass represents 85% of the measured IMPROVE PM<sub>2.5</sub> mass, ranging from 73 to 96%. The IMPROVE reconstructed mass contains a significant contribution (average of 29.6% and maximum of 64.9%) from fine soil.

Black carbon exhibited several elevated periods, above 4  $\mu\text{g m}^{-3}$ . Observations of low concentrations of PM<sub>2.5</sub> levoglucosan were used to rule out influence of biomass burning during the elevated BC periods. The methane mixing ratio, a regional tracer for O/G activity, was elevated during elevated BC periods, indicating O/G activity as a likely source of the polluted air mass. Gas flaring is common in the region and a likely source of the BC plumes detected.

Fine particle sulfate in the park was partially neutralized by ammonium. A period of acidic sulfate aerosol was observed early during the campaign while in other periods the apparent deficit of ammonium relative to sulfate concentrations was made up by the presence of calcium ion, likely reflecting a contribution from gypsum (CaSO<sub>4</sub>) found in regional soils. Under the hot,

dry conditions typical of the region in summer, ammonium nitrate formation is not favored. The summertime nitrate observed appears to be present as a result of abundant nitric acid reactions with both sea salt and calcium carbonate mineral dust. This finding is similar to previous reports from Big Bend National Park to the south [Lee et al., 2008]. Both gaseous  $\text{HNO}_3$  (avg  $0.89 \mu\text{g m}^{-3}$ ) and  $\text{NH}_3$  (avg  $0.93 \mu\text{g m}^{-3}$ ) were fairly abundant throughout the study, providing key reservoirs for further aerosol formation under the right conditions.

Aerosol light extinction was examined at both daily and hourly time resolution. At 24-hour timescales, light extinction values ranged from 19 to  $54 \text{ Mm}^{-1}$ , with a mean value of  $29 \text{ Mm}^{-1}$ . Considerably greater variability was observed at hourly timescales, reaching a maximum of  $90 \text{ Mm}^{-1}$  during the study. This temporal variability illustrates the importance of high time resolution measurements for understanding peaks in regional haze at protected locations. While  $\text{SO}_4^{2-}$ , on average, was the largest fine particle contributor to light extinction, BC, was found to dominate one of the haziest periods and soil dust was also an important contributor in many periods.

An analysis of transport patterns revealed that air masses with the highest concentrations of most aerosol constituents and those with the highest extinction values were transported predominantly from the southeast sector, a region with a high density of Permian Basin O/G operations. The prevalence of emissions transport from this region raises further concern regarding potential growth in haze impacts in the park if O/G activities and emissions continue to grow.

## 4.2 Future Research Directions

The primary goals of this work were to quantify  $\text{PM}_{2.5}$  in CAVE, provide insights into the composition and likely sources of  $\text{PM}_{2.5}$ , assess particulate matter haze impacts in CAVE, and determine source-receptor relationships for high concentration/light extinction air masses. This was accomplished by high time-resolution measurements of total and speciated  $\text{PM}_{2.5}$ , application of the IMPROVE second haze algorithm, and residence time analysis of HYSPLIT back trajectories.

Anticipated increases in O/G extraction in the area could further exacerbate the air quality problems documented during this study. This work effectively assessed the composition and con-

centration of aerosol species in CAVE, and provides insight into the likely sources of elevated  $PM_{2.5}$ . Several topics are ripe for further investigation:

- Source apportionment. Future work looking in more detail at source apportionment would be a valuable addition to understanding the relative impacts of specific emission sources. One useful addition would be to add higher time resolution measurements of the aerosol soil component, in particular, to understand the impacts of limestone and gypsum erosion on CAVE air quality. One could also combine study measurements of hourly, speciated VOCs with the aerosol observations to better characterize the influence of particular source types/regions on observed, polluted air masses. For example, increases in light alkane concentrations and decreases in the i-/n-pentane ratio could provide further evidence of O/G emissions in hazy air masses.
- Aerosol size distributions. Much of the interesting aerosol chemistry in the study involved either soil-related primary  $SO_4^{2-}$  emissions or reactions of nitric acid or its precursors with sea salt and soil dust. Speciated measurements of aerosol size distributions, e.g., using a MOUDI impactor, could provide greater insight into these interactions by better associating measured aerosol components with particle size. Evidence of these reactions, for example, is often found by comparing the size distribution of aerosol nitrate, from below 1 micron out to several microns, with those of  $Ca^{2+}$  and  $Na^+$ .
- Aerosol and haze during other seasons. This study focused exclusively on summertime haze, largely because the primary goal of CarCaVAQS was to examine conditions leading to elevated summertime ozone. The abundance of gaseous ammonia and nitric acid in the park, however, suggests that haze formation might be enhanced during cooler times of year via formation of ammonium nitrate.

Future work should also investigate changes to fine particulate matter concentration and composition as O/G development increases in the area.

# Appendix A

## USDA Census of Agriculture

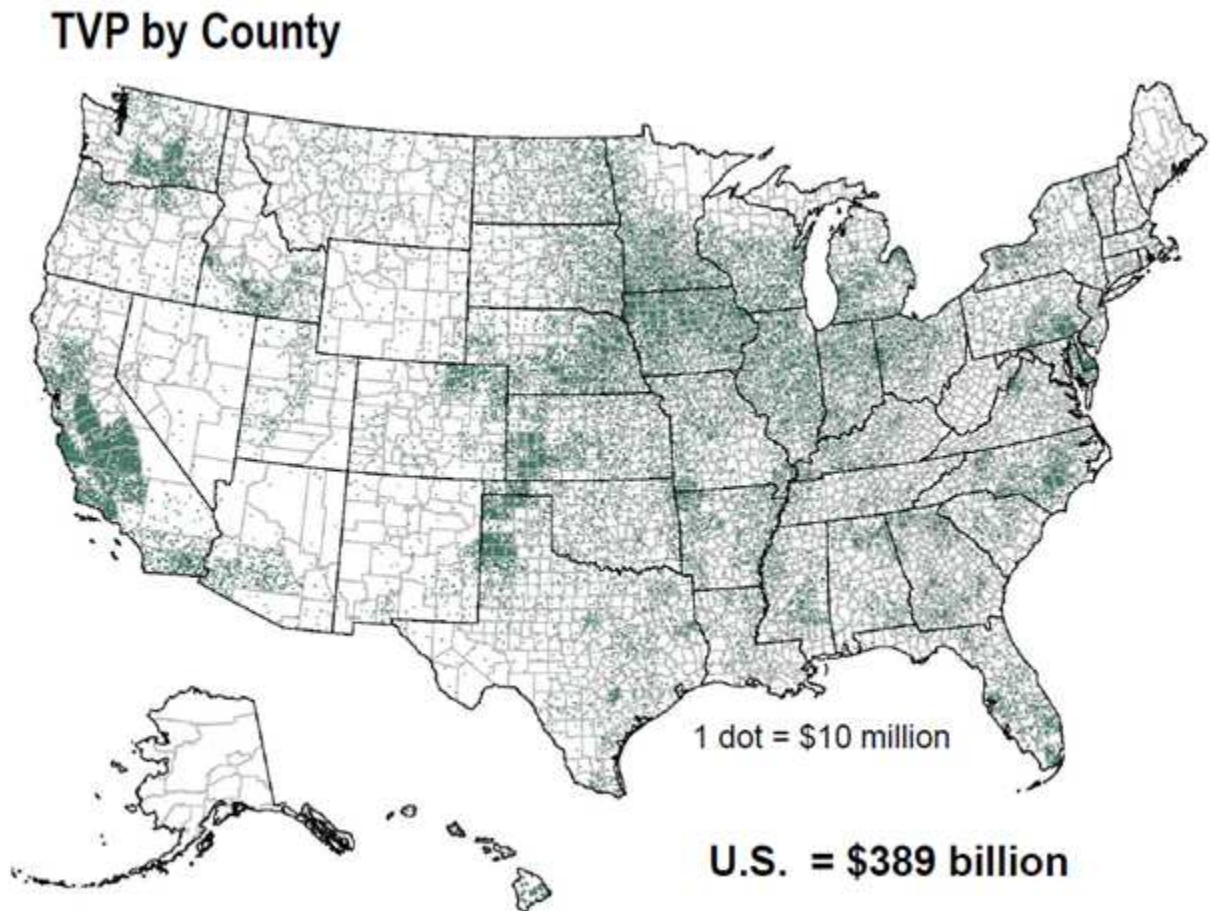


**Figure A.1:** Total Agricultural Production is shown from the USDA Census of Agriculture in 2017. Each green dot corresponds to 10 million USD in agricultural production. Data can be found at: [www.nass.usda.gov](http://www.nass.usda.gov)

# Appendix B

## Instrument Comparisons

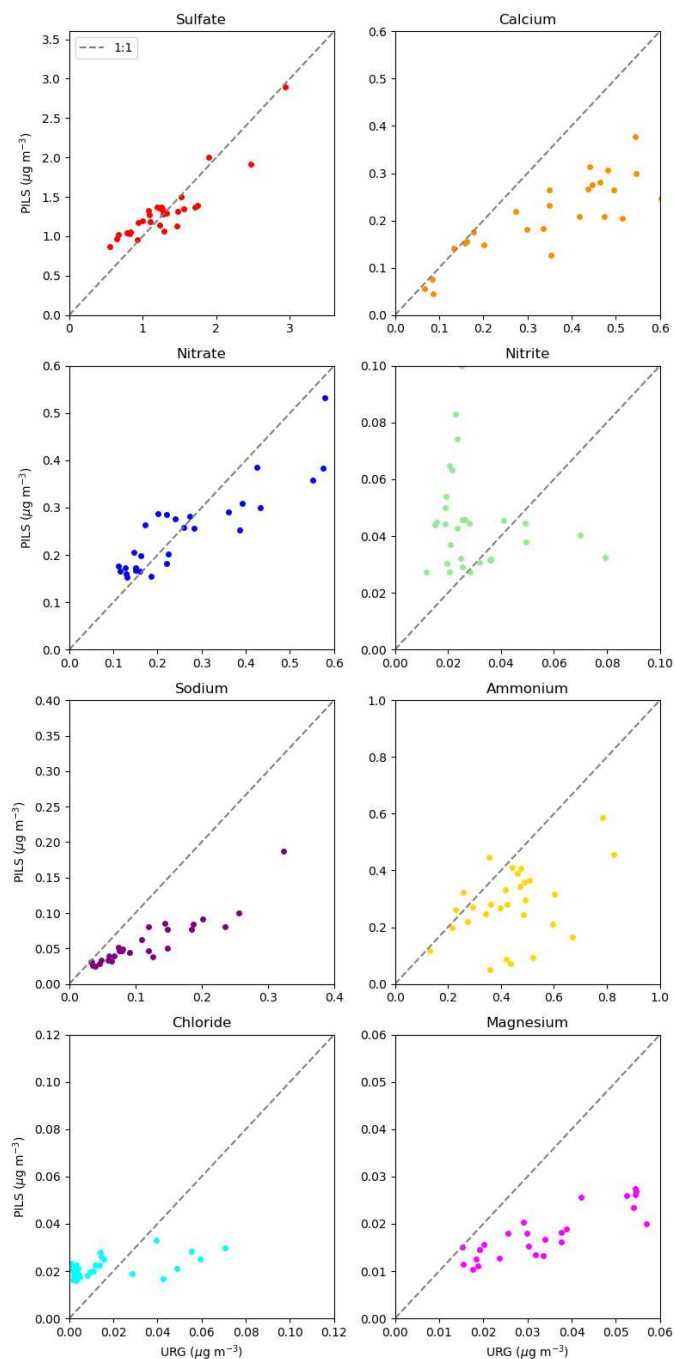


**Figure B.1:** Corresponding URG and PLS species are plotted at 24-hour time resolution. The PLS-IC data set was resampled to a daily mean. The dotted grey line has a slope of one and an intercept of zero.

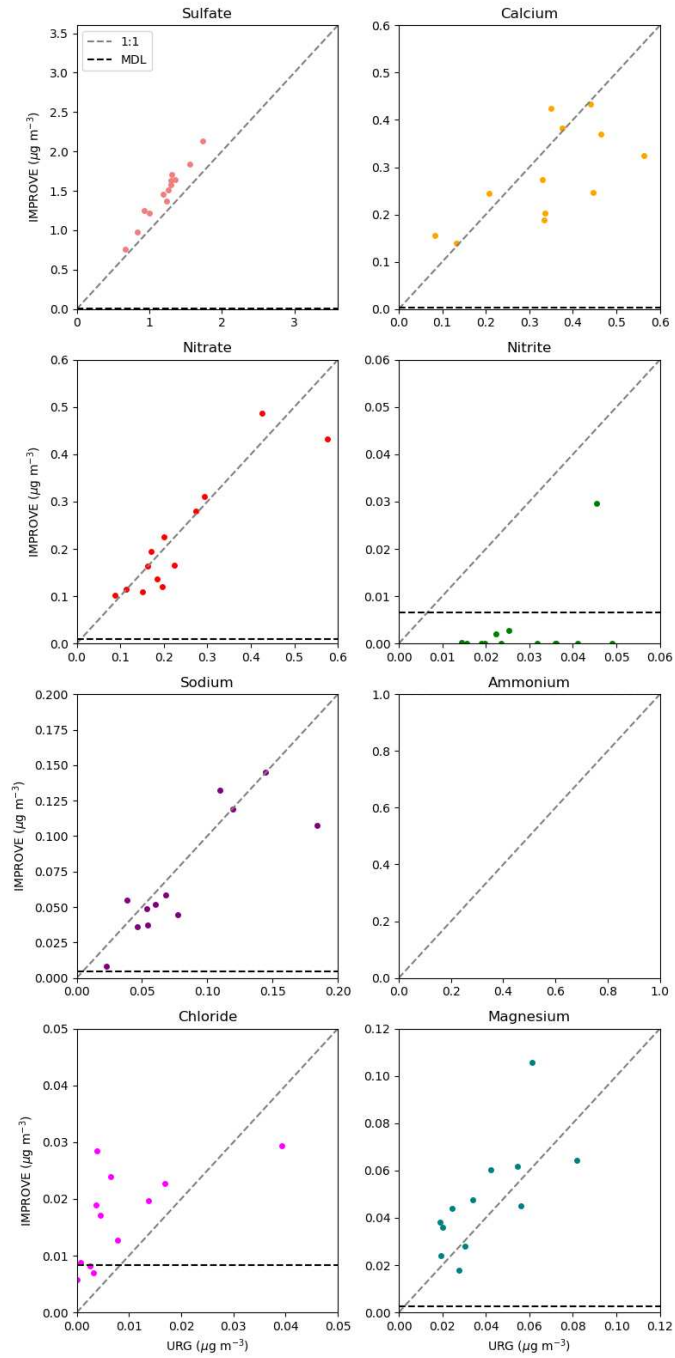


**Figure B.2:** Corresponding IMPROVE and PILS species are plotted at 24-hour time resolution. The dotted grey line has a slope of one and an intercept of zero.

## References

- Ahmadov, R., et al. (2015), Understanding high wintertime ozone pollution events in an oil- and natural gas-producing region of the western US, *Atmos. Chem. Phys.*, *15*(1), 411-429, doi:10.5194/acp-15-411-2015.
- Allen, D. T., D. Smith, V. M. Torres, and F. C. Saldaña (2016), Carbon dioxide, methane and black carbon emissions from upstream oil and gas flaring in the United States, *Current Opinion in Chemical Engineering*, *13*, 119-123, doi:https://doi.org/10.1016/j.coche.2016.08.014.
- Allegrini, I., F. De Santis, V. Di Palo, A. Febo, C. Perrino, M. Possanzini, and A. Liberti (1987), Annular denuder method for sampling reactive gases and aerosols in the atmosphere, *Science of The Total Environment*, *67*(1), 1-16, doi:https://doi.org/10.1016/0048-9697(87)90062-3.
- Allegrini, I., A. Febo, C. Perrino, and P. Masia (1994), Measurement of Atmospheric Nitric Acid in Gas Phase and Nitrate in Particulate Matter by means of Annular Denuders, *International Journal of Environmental Analytical Chemistry*, *54*(3), 183-201, doi:10.1080/03067319408034088.
- Attwood, A. R., et al. (2014), Trends in sulfate and organic aerosol mass in the Southeast U.S.: Impact on aerosol optical depth and radiative forcing, *Geophysical Research Letters*, *41*(21), 7701-7709, doi:https://doi.org/10.1002/2014GL061669.
- Bahreini, R., et al. Mass spectral analysis of organic aerosol formed downwind of the Deepwater Horizon oil spill: field studies and laboratory confirmations(1520-5851 (Electronic)).
- Benedict, K. B., C. M. Carrico, S. M. Kreidenweis, B. Schichtel, W. C. Malm, and J. L. Collett (2013), A seasonal nitrogen deposition budget for Rocky Mountain National Park, *Ecological Applications*, *23*(5), 1156-1169.
- Benedict, K. B., A. J. Prenni, M. M. H. El-Sayed, A. Hecobian, Y. Zhou, K. A. Gebhart, B. C. Sive, B. A. Schichtel, and J. L. Collett (2020), Volatile organic compounds and ozone at four national parks in the southwestern United States, *Atmospheric Environment*, *239*, 117783, doi:https://doi.org/10.1016/j.atmosenv.2020.117783.

Bond, T. C., et al. (2013), Bounding the role of black carbon in the climate system: A scientific assessment, *Journal of Geophysical Research: Atmospheres*, 118(11), 5380-5552., doi:<https://doi.org/10.1002/jgrd.50171>.

Bond, T. C., B. Wehner, A. Plewka, A. Wiedensohler, J. Heintzenberg, and R. J. Charlson (2006), Climate-relevant properties of primary particulate emissions from oil and natural gas combustion, *Atmospheric Environment*, 40(19), 3574-3587, doi:<https://doi.org/10.1016/j.atmosenv.2005.12.030>.

Brown, D., C. Lewis, and B. Weinberger (2015), Human exposure to unconventional natural gas development: A public health demonstration of periodic high exposure to chemical mixtures in ambient air, *Journal of Environmental Science and Health. Part A, Toxic/hazardous substances & environmental engineering*, 50, 460-472, doi:10.1080/10934529.2015.992663.

Burden, S., M. A. Cluff, L. E. Dehaven, C. Roberts, S. L. Sharkey, and A. Singer (May 2015), Review of State and Industry Spill Data: Characterization of Hydraulic Fracturing-Related Spills.

Böttcher, K., V.-V. Paunu, K. Kupiainen, M. Zhizhin, A. Matveev, M. Savolahti, Z. Klimont, S. Väätäinen, H. Lamberg, and N. Karvosenoja (2021), Black carbon emissions from flaring in Russia in the period 2012–2017, *Atmospheric Environment*, 254, 118390, doi:<https://doi.org/10.1016/j.atmosenv.2021.118390>.

Carter, W., and J. Seinfeld (2012), Winter ozone formation and VOC incremental reactivities in the Upper Green River Basin of Wyoming, *Atmospheric Environment*, 50, 255–266, doi:10.1016/j.atmosenv.2011.12.025.

Chow, J. C., J. G. Watson, L. W. A. Chen, M. C. O. Chang, N. F. Robinson, D. Trimble, and S. Kohl (2007), The IMPROVE\_A Temperature Protocol for Thermal/Optical Carbon Analysis: Maintaining Consistency with a Long-Term Database, *Journal of the Air & Waste Management Association*, 57(9), 1014-1023, doi:10.3155/1047-3289.57.9.1014.

Clegg, S. L., and J. H. Seinfeld (2004), Improvement of the Zdanovskii-Stokes-Robinson Model for Mixtures Containing Solutes of Different Charge Types, *The Journal of Physical Chemistry A*, 108(6), 1008-1017, doi:10.1021/jp030827q.

Conrad, B. M., and M. R. Johnson (2019), Mass absorption cross-section of flare-generated black carbon: Variability, predictive model, and implications, *Carbon*, 149, 760-771, doi:<https://doi.org/10.1016/j.carbon.2019.04.086>.

Duc, H. N., et al. (2020), Spatial-Temporal Pattern of Black Carbon (BC) Emission from Biomass Burning and Anthropogenic Sources in New South Wales and the Greater Metropolitan Region of Sydney, Australia, *Atmosphere*, 11(6), doi:10.3390/atmos11060570.

Edwards, P. M., et al. (2014), High winter ozone pollution from carbonyl photolysis in an oil and gas basin, *Nature*, 514(7522), 351-354, doi:10.1038/nature13767.

Elvidge, C. D., D. Ziskin, K. E. Baugh, B. T. Tuttle, T. Ghosh, D. W. Pack, E. H. Erwin, and M. Zhizhin (2009), A Fifteen Year Record of Global Natural Gas Flaring Derived from Satellite Data, *Energies*, 2(3), 595-622.

Evanoski-Cole, A. R., et al. (2017), Composition and sources of winter haze in the Bakken oil and gas extraction region, *Atmospheric Environment*, 156, 77-87, doi:<https://doi.org/10.1016/j.atmosenv.2017.02.019>.

Fairlie, T. D., D. J. Jacob, J. E. Dibb, B. Alexander, M. A. Avery, A. van Donkelaar, and L. Zhang (2010), Impact of mineral dust on nitrate, sulfate, and ozone in transpacific Asian pollution plumes, *Atmos. Chem. Phys.*, 10(8), 3999-4012, doi:10.5194/acp-10-3999-2010.

Fann, N., K. R. Baker, E. A. W. Chan, A. Eyth, A. Macpherson, E. Miller, and J. Snyder (2018), Assessing Human Health PM(2.5) and Ozone Impacts from U.S. Oil and Natural Gas Sector Emissions in 2025, *Environmental Science & Technology*, 52(15), 8095-8103, doi:10.1021/acs.est.8b02050.

Field, R. A., J. Soltis, M. C. McCarthy, S. Murphy, and D. C. Montague (2015), Influence of oil and gas field operations on spatial and temporal distributions of atmospheric non-methane hydrocarbons and their effect on ozone formation in winter, *Atmos. Chem. Phys.*, 15(6), 3527-3542, doi:10.5194/acp-15-3527-2015.

Fitz, D. R. (2002), Evaluation of Diffusion Denuder Coatings for Removing Acid Gases from Ambient Air. Final Report, Office of Air Quality Planning and Standards, U.S. Environmental Protection Agency. *Rep. NTIS/02925914*.

Fountoukis, C., and A. Nenes (2007), ISORROPIA II: a computationally efficient thermodynamic equilibrium model for  $\text{K}^+$ - $\text{Ca}^{2+}$ - $\text{Mg}^{2+}$ - $\text{NH}_4^+$ - $\text{Na}^+$ - $\text{SO}_4^{2-}$ - $\text{NO}_3^-$ - $\text{Cl}^-$ - $\text{H}_2\text{O}$  aerosols, *Atmos. Chem. Phys.*, 7(17), 4639-4659, doi:10.5194/acp-7-4639-2007.

Gaswirth, S. B., et al. (2018), Assessment of undiscovered continuous oil and gas resources in the Wolfcamp Shale and Bone Spring Formation of the Delaware Basin, Permian Basin Province, New Mexico and Texas, 2018, *Report Rep. 2018-3073*, Reston, VA.

Hecobian, A., et al. (2019), Air Toxics and Other Volatile Organic Compound Emissions from Unconventional Oil and Gas Development, *Environmental Science & Technology Letters*, 6(12), 720-726, doi:10.1021/acs.estlett.9b00591.

Hennigan, C. J., J. Izumi, A. P. Sullivan, R. J. Weber, and A. Nenes (2015), A critical evaluation of proxy methods used to estimate the acidity of atmospheric particles, *Atmos. Chem. Phys.*, 15(5), 2775-2790, doi:10.5194/acp-15-2775-2015.

Homeland Infrastructure Foundation-Level Data (HIFLD) (2019), *Oil and Natural Gas Wells*. Retrieved February 26, 2021, from <https://gii.dhs.gov/HIFLD>.

Johnson, K. S. (1997), Permian evaporites in the Permian basin of southwestern United States, *Prace - Panstwowego Instytutu Geologicznego*(157 PART 2), 95-96.

Jordan, C., J. Dibb, and B. Anderson (2003), Uptake of Nitrate and Sulfate on Dust Aerosols during TRACE-P, *Journal of Geophysical Research*, 108, doi:10.1029/2002JD003101.

Khalek, I. A., M. G. Blanks, P. M. Merritt, and B. Zielinska (2015), Regulated and unregulated emissions from modern 2010 emissions-compliant heavy-duty on-highway diesel engines, *Journal of the Air & Waste Management Association*, 65(8), 987-1001, doi:10.1080/10962247.2015.1051606.

Kim, P. S., et al. (2015), Sources, seasonality, and trends of southeast US aerosol: an integrated analysis of surface, aircraft, and satellite observations with the GEOS-Chem chemical transport model, *Atmos. Chem. Phys.*, 15(18), 10411-10433, doi:10.5194/acp-15-10411-2015.

Krueger, B. J., V. H. Grassian, A. Laskin, and J. P. Cowin (2003), The transformation of solid atmospheric particles into liquid droplets through heterogeneous chemistry: Laboratory insights into the processing of calcium containing mineral dust aerosol in the troposphere, *Geophysical Research Letters*, 30(3), doi:https://doi.org/10.1029/2002GL016563.

Lee, T., S. M. Kreidenweis, and J. L. Collett (2004), Aerosol Ion Characteristics During the Big Bend Regional Aerosol and Visibility Observational Study, *Journal of the Air & Waste Management Association*, 54(5), 585-592, doi:10.1080/10473289.2004.10470927.

Lee, T., X.-Y. Yu, B. Ayres, S. M. Kreidenweis, W. C. Malm, and J. L. Collett (2008), Observations of fine and coarse particle nitrate at several rural locations in the United States, *Atmospheric Environment*, 42(11), 2720-2732, doi:https://doi.org/10.1016/j.atmosenv.2007.05.016.

Liggio, J., S.-M. Li, A. Vlasenko, C. Stroud, and P. Makar (2011), Depression of Ammonia Uptake to Sulfuric Acid Aerosols by Competing Uptake of Ambient Organic Gases, *Environmental Science & Technology*, 45, 2790-2796, doi:10.1021/es103801g.

Liggio J, Li SM, Hayden K, Taha YM, Stroud C, Darlington A, Drollette BD, Gordon M, Lee P, Liu P, Leithead A, Moussa SG, Wang D, O'Brien J, Mittermeier RL, Brook JR, Lu G, Staebler RM, Han Y, Tokarek TW, Osthoff HD, Makar PA, Zhang J, Plata DL, Gentner DR. Oil sands operations as a large source of secondary organic aerosols. *Nature*. 2016 Jun 2;534(7605):91-4. doi: 10.1038/nature17646. Epub 2016 May 25. PMID: 27251281.

Lyon, D. R., R. A. Alvarez, D. Zavala-Araiza, A. R. Brandt, R. B. Jackson, and S. P. Hamburg (2016), Aerial Surveys of Elevated Hydrocarbon Emissions from Oil and Gas Production Sites, *Environmental Science & Technology*, 50(9), 4877-4886, doi:10.1021/acs.est.6b00705.

Malm, W. C., B. A. Schichtel, M. L. Pitchford, L. L. Ashbaugh, and R. A. Eldred (2004), Spatial and monthly trends in speciated fine particle concentration in the United States, *Journal of Geophysical Research: Atmospheres*, 109(D3), doi:https://doi.org/10.1029/2003JD003739.

Malm, W.C., Day, D.E., Carrico, C., Kreidenweis, S.M., Collett, J.L., McMeeking, G., Lee, T., Carrillo, J. and Schichtel, B. (2005). Intercomparison and closure calculations using measurements of aerosol species and optical properties during the Yosemite Aerosol Characterization Study. *Journal of Geophysical Research* 110: doi: 10.1029/2004JD005494. issn: 0148-0227.

Malm, W. C. (2016a), Chapter 1 - Introduction, in *Visibility*, edited by W. C. Malm, pp. 1-27, Elsevier, doi:<https://doi.org/10.1016/B978-0-12-804450-6.00001-2>.

Malm, W. C. (2016b), Chapter 2 - On the Nature of Light and Its Interaction with Atmospheric Particles, in *Visibility*, edited by W. C. Malm, pp. 29-72, Elsevier, doi:<https://doi.org/10.1016/B978-0-12-804450-6.00002-4>.

Malm, W. C., B. A. Schichtel, M. L. Pitchford, L. L. Ashbaugh, and R. A. Eldred (2004), Spatial and monthly trends in speciated fine particle concentration in the United States, *Journal of Geophysical Research: Atmospheres*, 109(D3), doi:<https://doi.org/10.1029/2003JD003739>.

McKenzie, L. M., R. Z. Witter, L. S. Newman, and J. L. Adgate (2012), Human health risk assessment of air emissions from development of unconventional natural gas resources, *Science of The Total Environment*, 424, 79-87, doi:<https://doi.org/10.1016/j.scitotenv.2012.02.018>.

Nenes, A., S. N. Pandis, and C. Pilinis (1998), ISORROPIA: A New Thermodynamic Equilibrium Model for Multiphase Multicomponent Inorganic Aerosols, *Aquatic Geochemistry*, 4(1), 123-152, doi:10.1023/A:1009604003981.

Nenes, A., S. N. Pandis, and C. Pilinis (1999), Continued development and testing of a new thermodynamic aerosol module for urban and regional air quality models, *Atmospheric Environment*, 33, 1553-1560.

Olaguer, E. P. (2012), The potential near-source ozone impacts of upstream oil and gas industry emissions, *Journal of the Air & Waste Management Association*, 62(8), 966-977, doi:10.1080/10962247.2012.688923.

Olaguer, E. P. (2017), Introduction: Definition of the Problem, in *Atmospheric Impacts of the Oil and Gas Industry*, edited by E. P. Olaguer, pp. xi-xii, Elsevier, Boston, doi:<https://doi.org/10.1016/B978-0-12-801883-5.00017-6>.

Oltmans, S., R. Schnell, B. Johnson, G. Pétron, T. Mefford, R. Neely, D. Helmig, and G. Pfister (2014), Anatomy of wintertime ozone associated with oil and natural gas extraction activity in Wyoming and Utah, *Elementa: Science of the Anthropocene*, 2.

Orsini, D., Y. Ma, A. Sullivan, B. Sierau, K. Baumann, and R. Weber (2003), Refinements to the Particle-Into-Liquid Sampler (PILS) for Ground and Airborne Measurements of Water Soluble Aerosol Composition, *Atmospheric Environment*, 37, 1243-1259, doi:10.1016/S1352-2310(02)01015-4.

Pandis, S. N., and J. H. Seinfeld (2016), *Atmospheric chemistry and physics: from air pollution to climate change*, Wiley-Blackwell.

Petzold, A., et al. (2013), Recommendations for the interpretation of "black carbon" measurements, *Atmospheric Chemistry and Physics*, 13, doi:10.5194/acpd-13-9485-2013.

Pitchford, M., W. Malm, B. Schichtel, N. Kumar, D. Lowenthal, and J. Hand (2007), Revised Algorithm for Estimating Light Extinction from IMPROVE Particle Speciation Data, *Journal of the Air & Waste Management Association*, 57(11), 1326-1336, doi:10.3155/1047-3289.57.11.1326.

Prenni, A., J. Hand, W. Malm, S. Copeland, G. Luo, F. Yu, N. Taylor, L. Russell, and B. Schichtel (2019), An examination of the algorithm for estimating light extinction from IMPROVE particle speciation data, *Atmospheric Environment*, 214, 116880, doi:10.1016/j.atmosenv.2019.116880.

Prenni, A. J., et al. (2016), Oil and gas impacts on air quality in federal lands in the Bakken region: an overview of the Bakken Air Quality Study and first results, *Atmos. Chem. Phys.*, 16(3), 1401-1416, doi:10.5194/acp-16-1401-2016.

Texas Commission on Environmental Quality (TCEQ). *Controlling HRVOC Emissions*. Retrieved November 11, 2021, from <https://www.tceq.texas.gov/airquality/stationary-rules/voc/hrvoc.html>.

Rappenglück, B., et al. (2014), Strong wintertime ozone events in the Upper Green River basin, Wyoming, *Atmos. Chem. Phys.*, 14(10), 4909-4934, doi:10.5194/acp-14-4909-2014.

Schnell, R. C., S. J. Oltmans, R. R. Neely, M. S. Endres, J. V. Molenaar, and A. B. White (2009), Rapid photochemical production of ozone at high concentrations in a rural site during winter, *Nature Geoscience*, 2(2), 120-122, doi:10.1038/ngeo415.

Shen, X., et al. (2021), Real-world emission characteristics of black carbon emitted by on-road China IV and China V diesel trucks, *Science of The Total Environment*, 799, 149435, doi:<https://doi.org/10.1016/j.scitotenv.2021.149435>.

Silvern, R., D. Jacob, P. Kim, E. Marais, and J. Turner (2016), Incomplete sulfate aerosol neutralization despite excess ammonia in the eastern US: a possible role of organic aerosol, *Atmospheric Chemistry and Physics Discussions*, 1-21, doi:10.5194/acp-2016-315.

Stein, A. F., R. R. Draxler, G. D. Rolph, B. J. B. Stunder, M. D. Cohen, and F. Ngan (2015), NOAA's HYSPLIT Atmospheric Transport and Dispersion Modeling System, *Bulletin of the American Meteorological Society*, 96(12), 2059-2077, doi:10.1175/BAMS-D-14-00110.1.

Subramanian, R., et al. (2015), Methane Emissions from Natural Gas Compressor Stations in the Transmission and Storage Sector: Measurements and Comparisons with the EPA Greenhouse Gas Reporting Program Protocol, *Environmental Science & Technology*, 49(5), 3252-3261, doi:10.1021/es5060258.

Sullivan, A., R. Weber, A. Clements, J. Turner, M. Bae, and J. Schauer (2004), A method for on-line measurement of water-soluble organic carbon in ambient aerosol particles: Results from an urban site, *Geophysical Research Letters*, 311, doi:10.1029/2004GL019681.

Sullivan, A. P., R. E. Peltier, C. A. Brock, J. A. de Gouw, J. S. Holloway, C. Warneke, A. G. Wollny, and R. J. Weber (2006), Airborne measurements of carbonaceous aerosol soluble in water over northeastern United States: Method development and an investigation into water-soluble organic carbon sources, *Journal of Geophysical Research: Atmospheres*, 111(D23), doi:<https://doi.org/10.1029/2006JD007072>.

Sullivan, A. P., A. S. Holden, L. A. Patterson, G. R. McMeeking, S. M. Kreidenweis, W. C. Malm, W. M. Hao, C. E. Wold, and J. L. Collett Jr. (2008), A Method for Smoke Marker Measurements and its Potential Application for Determining the Contribution of Biomass Burning from Wildfires and Prescribed Fires to Ambient PM<sub>2.5</sub> Organic Carbon, *Journal of Geophysical Research*, 113, D22302, doi:10.1029/2008JD010216.

Sullivan, A. P., et al. (2016), Evidence for ambient dark aqueous SOA formation in the Po Valley, Italy, *Atmos. Chem. Phys.*, 16(13), 8095-8108, doi:10.5194/acp-16-8095-2016.

Thompson, C. R., J. Hueber, and D. Helmig (2014), Influence of oil and gas emissions on ambient atmospheric non-methane hydrocarbons in residential areas of Northeastern Colorado, *Elementa: Science of the Anthropocene*, 3, doi:10.12952/journal.elementa.000035.

USDA National Agricultural Statistics Service, 2017 Census of Agriculture. Complete data available at [www.nass.usda.gov/AgCensus](http://www.nass.usda.gov/AgCensus).

United States Energy Information Administration (EIA). (2021a). *Where our natural gas comes from*. Retrieved November 11, 2021, from <https://www.eia.gov/energyexplained/natural-gas/where-our-natural-gas-comes-from.php>.

United States Energy Information Administration (EIA) (2021b). *Annual Energy Outlook*. Retrieved November 10, 2021, from <https://www.eia.gov/outlooks/aeo/>.

United States Energy Information Administration (EIA) (2022a). *U.S. Energy Mapping System*. Retrieved March 21, 2022, from <https://www.eia.gov/state/maps.php>.

United States Energy Information Administration (EIA) (2022b). *Total in Energy*. Retrieved March 21, 2022, from <https://www.eia.gov/todayinenergy/detail.php?id=29812>.

United States Energy Information Administration (EIA) (2022c). *U.S. Energy Mapping System*. Retrieved March 21, 2022, from <https://www.eia.gov/state/maps.php>.

United States Environmental Protection Agency (EPA). (1999). Regional Haze Regulations: Final Rule. 40 CFR Part 51, *Federal Register*, 64, 35714-35774.

Vengosh, A., R. B. Jackson, N. Warner, T. H. Darrah, and A. Kondash (2014), A Critical Review of the Risks to Water Resources from Unconventional Shale Gas Development and Hydraulic Fracturing in the United States, *Environmental Science & Technology*, 48(15), 8334-8348, doi:10.1021/es405118y.

Vidic, R., S. Brantley, J. Vandenbossche, D. Yoxheimer, and J. Abad (2013), Impact of Shale Gas Development on Regional Water Quality, *Science (New York, N.Y.)*, 340, 1235009, doi:10.1126/science.1235009.

Weber, R. J., D. Orsini, Y. Daun, Y. N. Lee, P. J. Klotz, and F. Brechtel (2001), A Particle-into-Liquid Collector for Rapid Measurement of Aerosol Bulk Chemical Composition, *Aerosol Science and Technology*, 35(3), 718-727, doi:10.1080/02786820152546761.

Wexler, A. S., and S. L. Clegg (2002), Atmospheric aerosol models for systems including the ions  $H^+$ ,  $NH_4^+$ ,  $Na^+$ ,  $SO_4^{2-}$ ,  $NO_3^-$ ,  $Cl^-$ ,  $Br^-$ , and  $H_2O$ , *Journal of Geophysical Research: Atmospheres*, 107(D14), ACH 14-11-ACH 14-14, doi:https://doi.org/10.1029/2001JD000451.

Wexler, A. S., and J. H. Seinfeld (1991), Second-generation inorganic aerosol model, *Atmospheric Environment. Part A. General Topics*, 25(12), 2731-2748, doi:https://doi.org/10.1016/0960-1686(91)90203-J.

Weyant, C. L., P. B. Shepson, R. Subramanian, M. O. L. Cambaliza, A. Heimbürger, D. McCabe, E. Baum, B. H. Stirn, and T. C. Bond (2016), Black Carbon Emissions from Associated Natural Gas Flaring, *Environmental Science & Technology*, 50(4), 2075-2081, doi:10.1021/acs.est.5b04712.

White, W. H., N. P. Hyslop, K. Trzepla, S. Yatkin, R. S. Rarig Jr, T. E. Gill, and L. Jin (2015), Regional transport of a chemically distinctive dust: Gypsum from White Sands, New Mexico (USA), *Aeolian research*, 16, 1-10.

Xiong, Y., J. Zhou, Z. Xing, and K. Du (2020), Optimization of a volatile organic compound control strategy in an oil industry center in Canada by evaluating ozone and secondary organic aerosol formation potential, *Environmental Research*, 191, 110217, doi:https://doi.org/10.1016/j.envres.2020.110217.

Yanowitz, J., R. L. McCormick, and M. S. Graboski (2000), In-Use Emissions from Heavy-Duty Diesel Vehicles, *Environmental Science & Technology*, 34(5), 729-740, doi:10.1021/es990903w.

Yu, X.-Y., T. Lee, B. Ayres, S. Kreidenweis, W. Malm, and J. Collett (2006), Loss of fine particle ammonium from denuded nylon filters, *Atmospheric Environment*, 40, 4797-4807, doi:10.1016/j.atmosenv.2006.03.061.

Yu, X.-Y., T. Lee, B. Ayres, S. M. Kreidenweis, J. L. Collett, and W. Malm (2005), Particulate Nitrate Measurement Using Nylon Filters, *Journal of the Air & Waste Management Association*, 55(8), 1100-1110, doi:10.1080/10473289.2005.10464721.

Zhang, Q., et al. (2007), Ubiquity and dominance of oxygenated species in organic aerosols in anthropogenically-influenced Northern Hemisphere midlatitudes, *Geophysical Research Letters*, 34(13), doi:<https://doi.org/10.1029/2007GL029979>.

Zimmerle, D., T. Vaughn, B. Luck, T. Lauderdale, K. Keen, M. Harrison, A. Marchese, L. Williams, and D. Allen (2020), Methane Emissions from Gathering Compressor Stations in the U.S, *Environmental Science & Technology*, 54(12), 7552-7561, doi:10.1021/acs.est.0c00516.